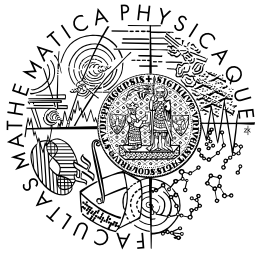

FACULTY
OF MATHEMATICS
AND PHYSICS
Charles University

MASTER THESIS

Martin Odehnal

The impacts that send meteoroids towards the Earth

Astronomical Institute of Charles University

Supervisor of the master thesis: doc. Mgr. Miroslav Brož, Ph.D.

Study programme: Astronomy a astrophysics

Prague 2025

I declare that I carried out this master thesis on my own, and only with the cited sources, literature and other professional sources. I understand that my work relates to the rights and obligations under the Act No. 121/2000 Sb., the Copyright Act, as amended, in particular the fact that the Charles University has the right to conclude a license agreement on the use of this work as a school work pursuant to Section 60 subsection 1 of the Copyright Act.

In ..... date ....

Author's signature

I would like to thank my supervisor for his patience, willingness to help, and infectious passion for the subject, which greatly motivated me throughout this work. I am also deeply grateful to my family for their unwavering support.

Title: The impacts that send meteoroids towards the Earth

Author: Martin Odehnal

Institute: Astronomical Institute of Charles University

Supervisor: doc. Mgr. Miroslav Brož, Ph.D.

Abstract: According to observations and radiometric signatures, 470 My ago, our planet witnessed a massive infall of L-chondrite meteorites. The only plausible source of these meteorites is a collision that created the asteroid family related to (20) Massalia (Marsset et al., 2024). Observations also show that 40 My ago, Massalia suffered another collision and formed a second overlapping family. Material from the more recent event makes up 37% of meteorite falls today. Using smoothed particle hydrodynamics (SPH) simulations, we investigated these two family-forming events. We assumed impacts into a monolithic body and then to a rubble-pile body. We were able to explain the observed size-frequency distribution of the Massalia family down to 1.5 km. If the distribution is extrapolated down to 100 μm, one can also account for observed 1.4° dust band (Nesvorný et al., 2006). The original asteroid size needed for extrapolation is from 134 km to 155 km. The shape of the largest remnant was compared to the recent adaptive-optics observations of (20) Massalia from the VLT/SPHERE instrument. Our rubble-pile model matches very well the observed shape.

Keywords: asteroids, (20) Massalia, meteorites, L chondrites, collisions, hydrodynamic simulations, SPH

Název práce: Impakty, které poslaly meteoroidy k Zemi

Autor: Martin Odehnal

Ústav: Astronomický ústav Univerzity Karlovy

Vedoucí: doc. Mgr. Miroslav Brož, Ph.D.

Abstrakt: Podle pozorování a radiometrických signatur před 470 My dopadaly L-chondritické meteority na naši planetu mnohem častěji než dnes. Jediným možným zdrojem těchto meteoritů je srážka, která vytvořila rodinu planetek spojovanou s planetkou (20) Massalia (Marsset et al., 2024). Pozorování rovněž ukazují, že před 40 My Massalia utrpěla další srážku a vytvořila druhou rodinu. Materiál z této pozdější události v současnosti tvoří 37 % všech pádů meteoritů. Pomocí hydrodynamických simulací jsme zkoumali tyto dvě události vedoucí ke vzniku rodin. Předpokládali jsme impakty do monolitického tělesa a následně do tělesa ze suti. Podařilo se nám vysvětlit pozorované rozdělení velikostí v rodině Massalia až do průměru 1,5 km. Pokud je toto rozdělení extrapolováno až do velikosti 100 μm, lze vysvětlit prachový pás pozorovaný na sklonu 1,4° (Nesvorný et al., 2006). Pro extrapolaci k prachu je potřeba, aby těleso mělo původní velikost 134 až 155 km. Tvar primárního těleso jsme porovnali s nedávným pozorováním planetky (20) Massalia adaptivní optikou přístroje VLT/SPHERE. Náš model ze suti odpovídá pozorovanému tvaru velmi dobře.

Klíčová slova: planetky, (20) Massalia, meteority, chondrity typu L, srážky, hydrodynamické simulace, SPH

Contents

Introduction

Asteroids are relatively small rocky bodies orbiting the Sun. They are the most numerous category of bodies in the Solar System (Jedicke et al., 2015). There are almost 1.5 million observed asteroids as of this moment, and many more, fainter, that remain unobserved (Jones et al., 2021). They can be found almost anywhere in the Solar System, but most of the observed ones orbit in the Main Belt, between ∼2.1 and 3.3 au. As they follow different intersecting orbits, they collide, albeit with a low probability. When they collide, they break, splinter, and eject debris, creating what is known as families.

Some fragments from collisions can travel from the main belt all the way to Earth and fall as meteorites. We are particularly interested in asteroid (20) Massalia and its associated family, which is the source of 37% of current meteorite falls (Marsset et al., 2024). Moreover, these L-chondrites exhibit shock ages of 470 My ago, indicating there was also a massive infall of meteorites originating from this family, which is likely tied to the mid-Ordovician ice age (Schmitz et al., 2019). Hereinafter, we investigate the impacts that created the Massalia family and sent meteoroids toward Earth.

This work is separated into 6 chapters. The first chapter serves as an introduction to asteroids and families, describing their orbits, physical properties, and mineralogy. The second chapter is an overview of physical processes governing impacts and the computational method (SPH) used for our simulations. The third chapter describes (20) Massalia itself and its associated family. The core of this work is in chapters four and five, where we discuss our simulations of impacts, both into a monolithic body and a rubble-pile body. Finally, in chapter six, we discuss an additional simulation: an impact into a layered body, with a monolithic core and a layer of rubble.

1 Asteroids and Families

1.1 Asteroids

Astronomers have been observing asteroids since the eighteen hundreds. In 1801, Italian astronomer Piazzi discovered the first asteroid (1) Ceres (Piazzi, 1802). Ever since then, we have come to observe millions of them in all parts of the Solar System, from the near-Earth space, with orbits crossing ours, to the far trans-Neptunian objects on the outskirts of the Solar System. The most readily observable are the Main belt asteroids, located between Mars and Jupiter, Trojans and Greeks orbiting Jupiter's Lagrangian points L5 and L4, Centaurs in the areas behind Jupiter, Neptune Trojans, Plutinos, and more. Hereinafter, we focus on the Main Belt, as the most observed and catalogued asteroids are located there.

Orbits Asteroids orbit the Sun, but they are also heavily influenced by other planets, especially Jupiter and Saturn. Their eccentricities and inclinations oscillate with amplitudes $\Delta e \approx 0.1 - 0.3$, $\Delta i \approx 5^\circ - 10^\circ$ and periods of the order of tens to hundreds of thousands of years. Thus, proper elements that are stable over millions of years are often used (Šidlichovský & Nesvorný, 1994).

Plotting the proper semimajor axis vs the proper eccentricity, or the proper inclination, shows a number of structures and properties. Looking at Fig. 1.1, there are immediately noticeable gaps between the populations. Those are called the Kirkwood gaps and are caused by mean-motion resonance with planets, especially Jupiter. A mean-motion resonance occurs when two bodies have mean motions that are simple integers of each other. The most notable include 3:1, 5:2, and 2:1 with Jupiter. These can destabilize the orbits by repeated perturbations, increasing the eccentricity until a close encounter with inner planets ejects them from the resonance. Secular resonances also occur when the precession of asteroids' orbits is synchronized with planets' orbits or more precisely, with fundamental frequencies of the N-planetary system.

Other than the motion induced by resonances, there are slow but steady dynamical effects that change asteroid orbits in the long term: the Yarkovsky and YORP effects (Vokrouhlický et al., 2015). These are thermal forces and torques, where the thermal emission from the asteroid and the asteroid's rotation cause the asteroid to move inwards or outwards.

In Fig. 1.1, the asteroids generally have high values of inclinations (and eccentricities) compared to planets; the origin of this is unknown, but it must be related to the early Solar System history, for example, to perturbation by migrating planetary embryos (e.g. Brož et al. (2021)).

Another structure highlighted in Fig. 1.1 is clumps of asteroids, or Hirayama families (Hirayama, 1918), which originated from asteroid collisions; more on them later, in Sec. 1.2.

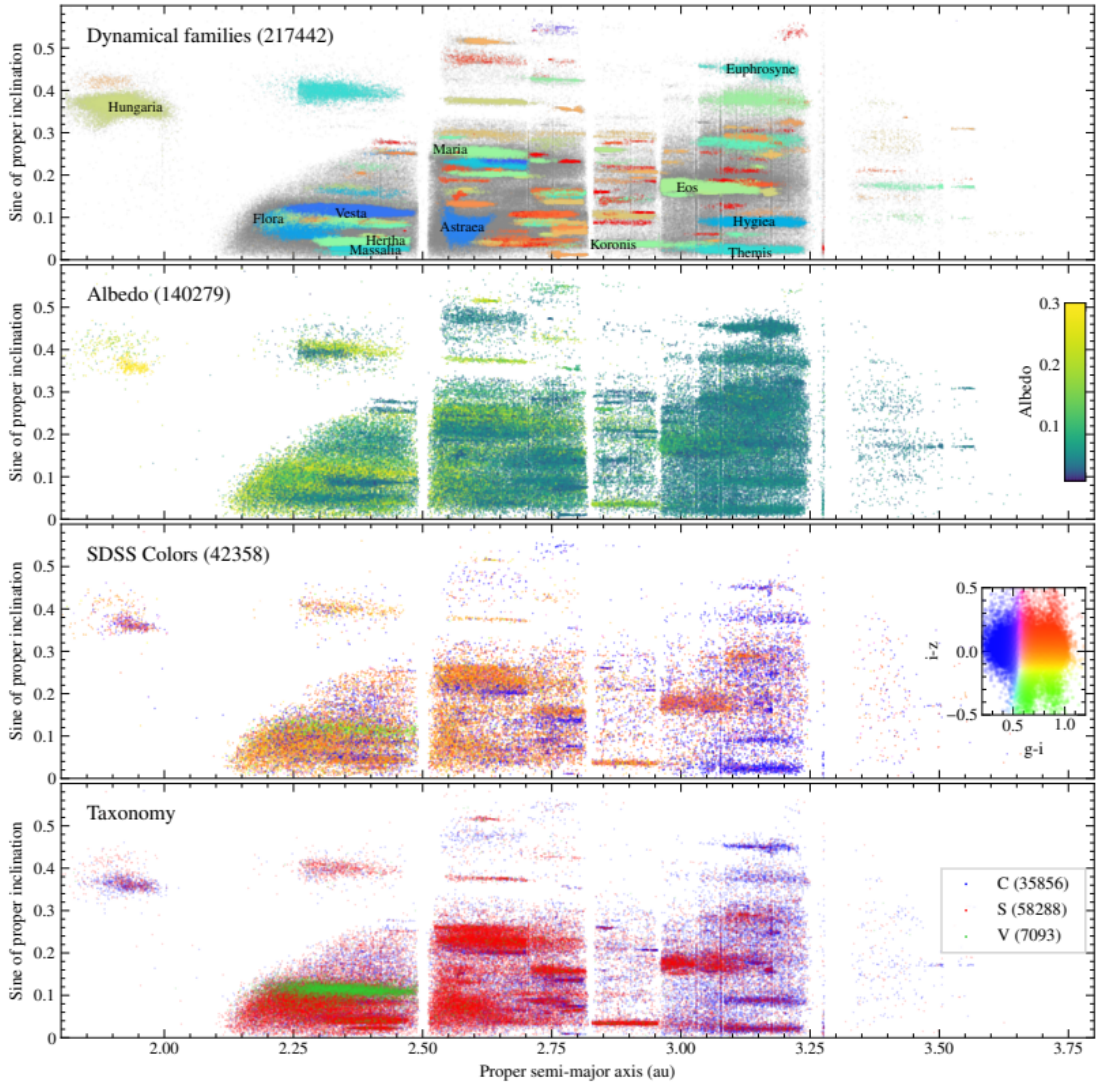

Figure 1.1 Proper elements (semimajor axis and sine of inclination) of asteroids in the Main Belt showing in color distribution of families (first), albedo (second), color indices (third), and taxonomy (fourth). Brackets specify numbers of plotted objects. Image taken from Berthier et al. (2023).

Nevertheless, here we discuss mechanisms that can accelerate asteroids and change their orbits. One can calculate how the orbital elements change when an acceleration acts on an asteroid using the Gauss equations:

$$\frac{\mathrm{d}a}{\mathrm{d}t} = \frac{2}{n\sqrt{1-e^2}} \left[eR \sin f + T(1 + e\cos f)\right], \tag{1.1}$$

$$\frac{\mathrm{d}e}{\mathrm{d}t} = \frac{\sqrt{1-e^2}}{an}[R \sin f + T(\cos f + \cos E)], \tag{1.2}$$

$$\frac{\mathrm{d}I}{\mathrm{d}t} = \frac{N}{na\sqrt{1-e^2}} \frac{r}{a} \cos(\omega + f), \tag{1.3}$$

where R, T and N denote the components of acceleration: radial, transversal and normal. n is the mean motion, f, the true anomaly, E, the eccentric anomaly and ω, the argument of periapsis.

Physical Properties Asteroids come in all manner of shapes and sizes. In size, they vary from bodies almost 1000 km in diameter ((1) Ceres) to meter-sized meteoroids, regolith (mm to cm) and tiny dust particles (100 μm). The shapes range from near-spherical to highly elongated or otherwise irregular. One common shape is the "diamond-like," observed in-situ for Ryugu and Bennu, influenced by their spin and surface regolith migration (Bottke et al., 2024). These are asteroids from the NEO space region that were visited by the spacecraft Hayabusa and OSIRIS-REx.

Other than direct imaging, one can observe by means of light curves, from which one can subsequently derive a shape and rotational state, using the inversion method (Kaasalainen & Torppa, 2001). An example of a database for such models is DAMIT (Ďurech et al., 2018). Alternatively, a shape model can also be obtained by radar Doppler imaging, which provides detailed models for near-Earth asteroids (Kruzins et al., 2024). Finally, one can observe by means of adaptive optics (AO) and deconvolution (Vernazza et al., 2021).

Most asteroids rotate with rotational periods between 2 and 20 hours (Pravec et al., 2002). In fact, no large asteroids rotate faster than the 2.2-hour limit. If an asteroid spins faster than this critical period, the surface speed from rotation would be higher than the Kepler speed, and an asteroid would eject mass from its surface. However, there are examples of small asteroids (D<200 m) which exhibit cohesive strength and withstand spinning faster than the critical period. Both fast and slow rotators have the same likely origin: the YORP effect (Vokrouhlický et al., 2004), which generates torque due to anisotropic emission of thermal radiation.

Although there are no large, fast-rotating asteroids, not all asteroids are rubble piles. Holsapple & Michel (2008) shows that no known material strength is sufficient to withstand centrifugal disruption at high rotation rates. However, many small asteroids, those spinning faster than the critical period, are monolithic, while the remainder are likely rubble piles. A common structure among asteroids is that of a gravitational aggregate composed of smaller fragments, often with

significant voids between them (Walsh, 2018). Such voids and macroporosity can exceed 40%, as observed for asteroids, e.g. Bennu and Ryugu (Bottke et al., 2024).

Spectral Types and Mineralogy Asteroid mineralogy is primarily studied with reflectance spectroscopy, which links spectral features to specific minerals such as olivine ($(Mg, Fe)_2SiO_4$), forsterite (Mg_2SiO_4), fayalite (Fe_2SiO_4), orthopyroxene ($(Mg, Fe)SiO_3$), ferrosilite ($FeSiO_3$), enstatite ($MgSiO_3$), etc. The most notable absorption bands are for the olivine at 1.05 μm and for the pyroxene at 0.9 and $\sim$2.0 μm. This enables us to estimate mineral composition and abundance on asteroidal surface. However, some bodies, especially carbon-rich ones, are more difficult to interpret in this way (Rubin & Ma, 2017).

Based on the reflectance spectra, asteroids are classified into spectral types DeMeo et al. (2009). There are 28 types in total, but the most notable in the main belt are S-, C-, X- and D-types. S-complex spectra are silicate, typically have moderate albedo ($\sim$ 0.2-0.3), and are linked to ordinary chondrites (Brož et al., 2024; Marsset et al., 2024). Notable members include (8) Flora, (15) Eunomia, (20) Massalia, (158) Koronis, or (433) Eros. C-complex asteroids are carbonaceous, dark ($0.05 - 0.1$), and often show signs of hydration. Notable members include (1) Ceres, (2) Pallas, or (10) Hygiea. X-complex asteroids exhibit nearly featureless spectra and a wide range of albedos, from bright E-types ($\sim$ 0.4) to dark P-types ($\sim$ 0.05), reflecting diverse mineralogies that may include metallic iron, enstatite, or primitive silicates. D-type asteroids are very dark ($\sim$ 0.04), with red, featureless spectra that suggest a composition rich in organics and possibly ices; they are common in the outer main belt and among Jupiter Trojans. As shown in Fig. 1.1, the populations change with the distance from the Sun, with S-types dominating at distances $\leq$ 2.5 au and C-types becoming prevalent at $\geq$ 2.5 au.

Scaling Law An important issue tied to the asteroid's inner structure and strength is the scaling law. It governs asteroid impacts and relates the energy of impact to size and material properties of the target, using the quantity Q_D^*. This quantity, called the critical impact specific energy, represents the energy per unit mass delivered by the projectile, which is required for catastrophic disruption of the target (such that one half of the mass of the target escapes to infinity). It depends on both material strength and gravitational binding. The strength is more significant for small asteroids, while large ones are governed by self-gravity. Fig. 1.2 shows that the transition between the two regimes occurs at the size 100 to 200 m, which are the weakest bodies in our Solar System (Bottke et al., 2015).

1.2 Families

Over a century ago, Hirayama (1918) identified groups of asteroids with similar orbital elements, hinting at the groups' common origin. These groups are now known as asteroid families and are interpreted as fragments from a single or more collisions. Families are primarily found in the Main Belt, and their presence and formation reveal major impact events happening throughout the Solar System's history (Bottke et al., 2015; Nesvorný et al., 2015).

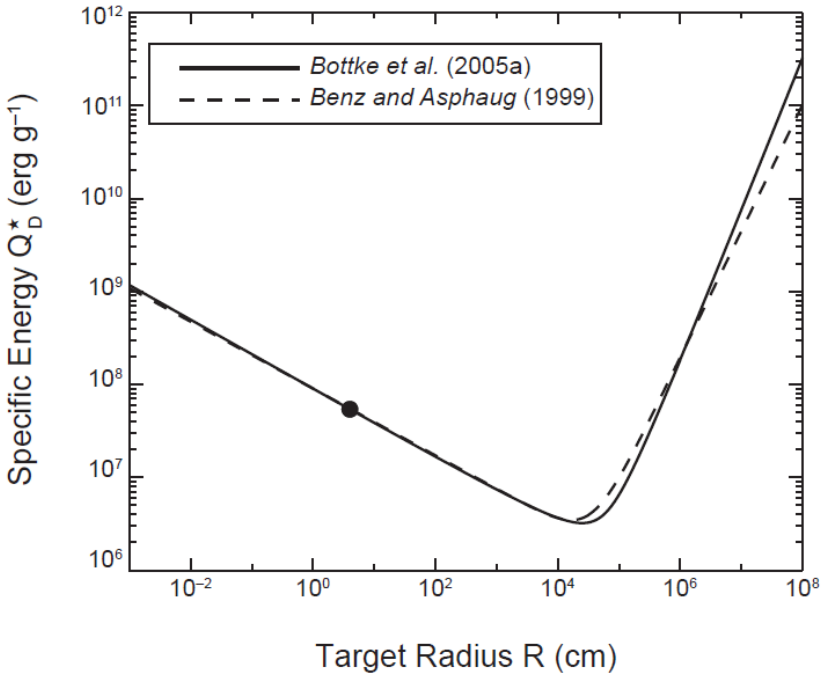

Figure 1.2 The critical impact specific energy Q^*_D vs. target radius, defined by Benz & Asphaug (1999) and Bottke et al. (2005). The transition from from strength regime to gravity regime occurs around $\sim 100 - 200$ m. Image taken from (Bottke et al. (2015))

Once formed, asteroid families do not remain static. They dynamically evolve under the influence of gravitational perturbations and non-gravitational forces, in particular the Yarkovsky effect (Vokrouhlický et al., 2015). As the family ages, it spreads in orbital element space, and if it is sufficiently stretched towards resonances, it delivers some bodies to near-Earth orbits. Knowing this, performing a backwards integration and finding the convergence of individual orbits is possible for the youngest families and, hence, estimating their age (Nesvorný & Bottke, 2004).

Beyond the dynamics, asteroid families allow us to study the interiors of the respective parent bodies. Revealing and preserving the inner mineral composition, otherwise inaccessible deep within the parent body (Masiero et al., 2015).

In two break-through papers, Brož et al. (2024) and Marsset et al. (2024) demonstrated that about ∼70% of all meteorites that currently fall to Earth originate from just three recent breakups, which occurred 5.8, 7.6, and ∼40 My ago. They are associated with the asteroids (832) Karin, (158) Koronis, and (20) Massalia, respectively. In this work, we modeled the breakup of (20) Massalia.[1]

Size-Frequency Distribution An important tool for describing asteroid families is the size-frequency distribution (SFD). It describes the number of fragments of different sizes in an asteroid family. It is typically plotted as the cumulative number, $N(>D)$ vs. diameter D on a log-log scale.

[1]see `https://sirrah.troja.mff.cuni.cz/~mira/lchondrites/`

Often, some parts of the SFD can be approximated by a power-law:

$$N(>D) \approx cD^b, \tag{1.4}$$

where the slope b is typically steep right after a catastrophic collision, for the kilometer sizes. With time, it becomes more shallow, through subsequent collisions, and stabilizes at $b \approx$-2.5 by the collisional cascade (Dohnanyi, 1969). The slope then remains the same; only the total population reduces.

A detailed look into the possible shapes of the SFD shortly after impact is in Durda et al. (2007); Ševeček et al. (2017, 2019); Benavidez et al. (2018). Using SPH simulations, they show how the SFD changes with growing impact energy (Q, or v, or d) and the impact angle. For low-energy impacts, e.g., cratering, the SFD is typically concave, with the largest remnant much larger than the largest fragment. As the impact energy increases for catastrophic events, the SFD becomes convex, with the largest remnant similar in size to the largest fragment.

For further details about the known asteroid families, including their physical properties, see Masiero et al. (2015); Nesvorný et al. (2015, 2024).

2 Dynamics of Collisions

In this work, we modeled asteroid collisions and family formation. To do so, we used the Opensph code by Ševeček et al. (2019); Ševeček (2021). It is based on the smooth particle hydrodynamics (SPH) method. The code allows for thorough simulations of all relevant physical processes happening during such impacts, ranging from compression, decompression, deformation, vaporization, shock wave, rarefaction wave, expansion, ejection, self-gravity, reaccumulation, friction, bouncing, merging, to binary formation.

2.1 Equations of Motion

While modeling the impacts, we solve the equations of motion in Lagrangian form. The set includes the continuity equation:

$$\frac{\mathrm{d}\rho}{\mathrm{d}t} = -\rho\nabla\cdot\boldsymbol{v}, \tag{2.1}$$

the Navier-Stokes equation:

$$\frac{\mathrm{d}\mathbf{v}}{\mathrm{d}t} = -\frac{1}{\rho}\nabla P - \nabla\Phi + \frac{1}{\rho}\nabla\cdot\mathbf{S}, \tag{2.2}$$

the first law of thermodynamics:

$$\frac{\mathrm{d}U}{\mathrm{d}t} = -P\nabla\cdot\mathbf{v} + \mathbf{S} : \tfrac{1}{2}\left[\nabla\mathbf{v} + (\nabla\mathbf{v})^T\right] \tag{2.3}$$

and the Poisson equation:

$$\nabla^2\Phi = 4\pi G\rho, \tag{2.4}$$

with ρ standing for the density, $\mathbf{v}$, velocity, P, pressure, $\mathbf{S}$, stress tensor, U, internal energy, and Φ, gravitational potential.

2.2 Equation of State

The equation of state commonly used in impact simulations is the Tillotson equation (Tillotson, 1962):

$$P = \begin{cases} A(\frac{\rho}{\rho_0}-1) + B(\frac{\rho}{\rho_0}-1)^2 + a\rho U + \frac{b\rho U}{\frac{U}{U_0}+1} & \text{for } U < U_{\mathrm{iv}}, \\ a\rho U + \left[\frac{b\rho U}{\frac{U}{U_0}+1} + A(\frac{\rho}{\rho_0}-1)e^{-\beta(\frac{\rho_0}{\rho}-1)}\right] e^{-\alpha(\frac{\rho_0}{\rho}-1)} & \text{for } U > U_{\mathrm{cv}}, \end{cases} \tag{2.5}$$

where ρ_0 is density at zero pressure, U_0 the internal energy at zero pressure, U_{iv} at the initial evaporation, U_{cv} at complete evaporation. A, B, a, b, α, β are material parameters of the state equation. The equation defines pressure P separately for material before evaporation and after it completely evaporates. In the case where the material has already begun to evaporate but has not evaporated completely, linear interpolation between pressures is used (Benz & Asphaug, 1993).

2.3 Rheology

The evolution of the stress tensor $\mathbf{S}$ is described by the constitutive relation and it is generally different for fluids and solids. In fluids, the stress tensor is parametrized by the viscosity:

$$\mathbf{S} = \mu_1 \left[\nabla\mathbf{v} + (\nabla\mathbf{v})^T\right] + \left(\mu_2 - \tfrac{2}{3}\mu_1\right)(\nabla\cdot\mathbf{v})\mathbf{I}, \tag{2.6}$$

here μ_1 is the dynamical viscosity, μ_2 the volumetric viscosity, $\mathbf{I}$ the unity matrix.

For solids, the simplest relation is Hook's law:

$$\frac{\mathrm{d}\mathbf{S}}{\mathrm{d}t} = \mu_1 \left[\nabla\mathbf{v} + (\nabla\mathbf{v})^T\right] + \left(\mu_2 - \tfrac{2}{3}\mu_1\right)(\nabla\cdot\mathbf{v})\mathbf{I}. \tag{2.7}$$

In this case, the right-hand side is in principle the same as for fluids, however, whereas in fluids the stress tensor could be computed directly, in solids, it must be integrated in time from specified initial conditions.

The applicability of Hook's law is limited only to low stresses and small deformations. When modeling highly energetic events, such as asteroid impacts, it becomes necessary to account for more complex rheological behavior that incorporates plasticity and failure, such as the von Mises or Drucker-Prager yield criteria.

Von Mises Criterion The simpler of the two, described in Mises (1913), has a single parameter: the plasticity limit Y_0, which is the upper limit of elastic deformations. When the stress reaches the limit, it does not increase any further; only the strain increases, and the deformation becomes plastic. Mathematically:

$$\mathbf{S} = f, \quad f = \min\left(\frac{Y_0}{\sqrt{\frac{3}{2}\mathbf{S}:\mathbf{S}}}, 1\right). \tag{2.8}$$

A fragmentation model can be directly incorporated into the von Mises criterion, using the scalar damage D, like so:

$$Y = (1 - D)Y_0. \tag{2.9}$$

Under this description, fully damaged material ($D = 1$) has no stress and behaves as an ideal fluid. However, such material fails to describe granular materials due to the absence of dry friction.

Drucker-Prager Criterion A better model for bodies of granular material is the Drucker-Prager model (Collins et al., 2004; Jutzi et al., 2015). This model describes the yield strength for intact and damaged rock separately:

$$Y_\mathrm{i} = Y_0 + \frac{\mu_\mathrm{i} P}{1 + \mu_\mathrm{i} P/(Y_\mathrm{M} - Y_0)}, \tag{2.10}$$

$$Y_\mathrm{d} = \mu_\mathrm{d} P, \tag{2.11}$$

where Y_0 is the cohesion, μ_i is the coefficient of internal friction, μ_d is the coefficient of dry friction and Y_M is the von Mises plasticity limit. Under this model, the material has non-zero strength even in the fully damaged state. This allows the material to form structures under constant gravity, whereas the von Mises material cannot.

Fragmentation Another material characteristic we have to consider is failure under deformation. When strain passes a threshold or strength limit, cracks appear and start to grow. The cracks originate in tiny flaws and grow approximately at half the speed of sound.

Grady & Kipp (1980) introduced damage D to describe the activation of flaws and the propagation of cracks. It is $0 \leq D \leq 1$ and represents the degree of fragmentation. The damage modifies the pressure P and the stress tensor $\mathbf{S}$ as:

$$P^* = \begin{cases} P & \text{for } P \geq 0, \\ (1-D)P & \text{for } P \leq 0, \end{cases} \tag{2.12}$$

$$\mathbf{S}^* = (1-D)\mathbf{S}. \tag{2.13}$$

The concentration and distribution of flaws is described by the Weibull distribution (Weibull, 1939). It describes the number of flaws in unit volume whose activation threshold is lower than ϵ:

$$N(<\epsilon) = k\epsilon^m, \tag{2.14}$$

where k and m are the Weibull coefficients, specific for a given material.

2.4 SPH Method

The SPH method was originally developed by Lucy (1977) and Gingold & Monaghan (1977). Libersky & Petschek (1991) and Jutzi et al. (2015) adapted the method for simulations of solid bodies and, more specifically, asteroid collisions. I will introduce the main principles behind the method, drawing from the SPH review by Springel (2010), Ševeček (2021) and Brož & Šolc (2013).

The main idea behind SPH is to treat hydrodynamics in a completely mesh-free fashion, using a set of particles. It is a Lagrangian method, where the continuum is discretized into a finite number of particles. The density is determined by the number of particles in a given volume, while each particle has its associated quantities and fixed mass. The particles then interact with one another, allowing for natural changes in topology of simulated fluid. They act as "tracers", moving with the velocities of the continuum and propagating the associated quantities.

Kernel Interpolant The core of the method is the kernel interpolant. To obtain it for a generic field $F(r)$, we start with convolution with the Dirac distribution δ:

$$F(r) = \int_\Omega F(r')\delta(r-r')\mathrm{d}r'. \tag{2.15}$$

If we then replace the δ distribution with a smoothing function $W(r)$, called kernel, we obtain an approximation:

$$F(r) \doteq \int_\Omega F(r')W(r-r',h)\mathrm{d}r', \tag{2.16}$$

where h is the smoothing length, and its limit $h \to 0$ is the δ function. Suppose we know the field at a set of points, $F_i = F(r_i)$, and each point has associated mass m_i and density ρ_i. We can then approximate the integral with the sum

$$F(r) = \sum_j \frac{m_j}{\rho_j} F_j W(r-r_j,h). \tag{2.17}$$

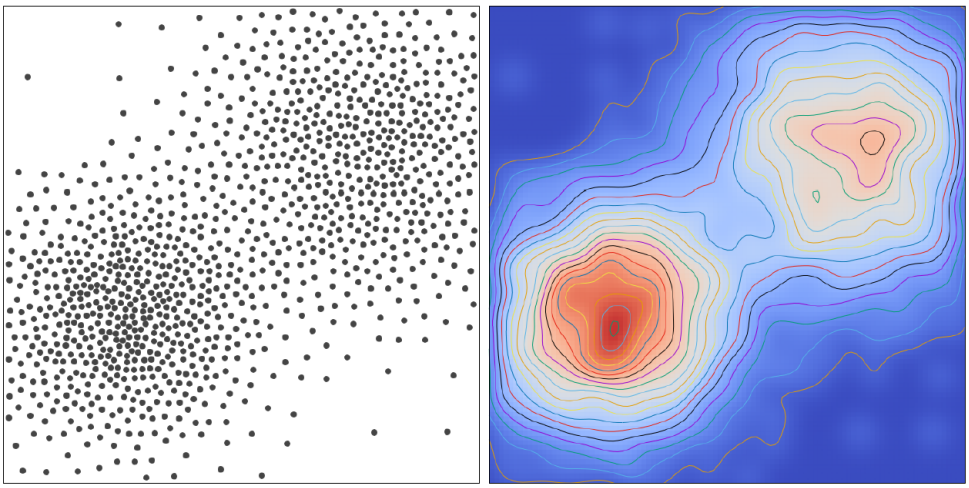

Figure 2.1 An illustration from Ševeček (2021) of continuum density computed from a discrete collection of particles scattered in space. The left image shows the particles themselves, while the right image shows the interpolated density. Calculated using Eq. 2.18, plotted with color gradients and contour lines.

Note, the estimate for $F(r)$ is defined everywhere, not just a set of points.

If we set $F(r) = \rho(r)$ we get the expression for computing density:

$$\rho(r) = \sum_j m_j W(r - r_j, h). \tag{2.18}$$

Fig. 2.1 shows this in visual form.

The general kernel interpolation technique can be applied to all other fields and differential operators. For example, we could write the divergence of velocity as:

$$(\nabla \cdot v)_i = \sum_j \frac{m_j}{\rho_j} v_j \nabla_i W(r_i - r_j, h). \tag{2.19}$$

The Kernel W should ideally be normalized, compact, symmetric, positive, strictly decreasing, and smooth. The most commonly used kernel is called the cubic spline and is defined as:

$$W(R,h) = \frac{3}{2\pi h} \begin{cases} \frac{2}{3} - 4R^2 + 4R^3 & \text{for } 0 \leq R < \frac{1}{2}, \\ \frac{4}{3} - 4R + 4R^2 - \frac{4}{3}R^3 & \text{for } \frac{1}{2} \leq R < 1, \\ 0 & \text{for } R \geq 1. \end{cases} \tag{2.20}$$

Artificial Viscosity A problem arises if we need to model shock waves, which would imply jumps in quantities and infinite gradients. This problem is solved by adding the artificial viscosity (Monaghan, 1989), defined as:

$$\Pi_{ij} = \begin{cases} \dfrac{-\alpha c_{ij} \mu_{ij} + \beta \mu_{ij}^2}{\rho_{ij}}, & \text{if } \mathbf{v}_{ij} \cdot \mathbf{r}_{ij} < 0, \\ 0, & \text{otherwise}, \end{cases} \tag{2.21}$$

with:

$$\mu_{ij} = \frac{h_{ij}\,\mathbf{v}_{ij}\cdot\mathbf{r}_{ij}}{|\mathbf{r}_{ij}|^2 + \epsilon h^2}, \tag{2.22}$$

where h_{ij} and ρ_{ij} are the arithmetic means of corresponding quantities for two particles i and j, and c_{ij} is the mean sound speed. Typical values for parameters are $\alpha = 1.5$, $\beta = 3$, $\epsilon = 0.01$. Using artificial viscosity, we effectively achieve convergence at the cost of resolution.

Self-Gravity is extremely important in asteroid collisions. Since in the scaling law (Benz & Asphaug, 1999), the transition from the strength regime to the gravity regime occurs at $D = 100\,\mathrm{m}$, and it is especially vital in the reaccumulation phase after impact. However, it is a long-distance force that needs integration over all particles. This would cause the algorithm to be of $O(N^2)$ complexity, making simulations with $N \geq 10^4$ particles very time-consuming.

To calculate gravity efficiently, the tree-method algorithm by Barnes (1986) is used. The algorithm works by providing a hierarchical grouping of particles. It effectively replaces far-away groups of particles with a single particle in the center of mass of the group, thus reducing the effective number of gravitational interactions. Using this algorithm reduces the complexity to $O(N\log N)$.

3 Observations

The asteroids we are mostly interested in are the (20) Massalia and its associated family. They are located in the inner region of the Main Belt, around 2.41 au at low eccentricities ($e = 0.16$) and low inclinations ($I = 1.4\ ^\circ$) (Mozovitz et al. 2022). The family is also highlighted in Fig. 1.1.

3.1 (20) Massalia

The primary body is the asteroid (20) Massalia. It was discovered in 1852 by Annibale de Dasparis and Jean Chacornac and takes its name from the French city of Marseilles.

Physical Properties The current model of Massalia assumes a diameter of 131.56 km, which puts it among the hundred largest asteroids. (Marsset et al., 2024) According to spectroscopy, it belongs among S-type asteroids (Mahlke et al., 2022), which means it's made of silicate materials, such as olivine and pyroxene. S-types are also the most common type at 2.41 au, where (20) Massalia is located. From the pyroxene to olivine ratio (ol/(ol+opx) = 65%) and band profiles, its mineralogy is likely L-chondrite-like (Marsset et al., 2024). The albedo is 0.20±0.04 (Berthier et al., 2023), which is also typical for S-types. The estimated density of $2700\,\mathrm{kg/m^3}$, was derived from the estimated mass $(4.3 \pm 0.5) \cdot 10^{18}\,\mathrm{kg}$ (Berthier et al., 2023). The asteroid is rotating around its principal axis with a period of 8.1 hours and 48.9° obliquity (Cellino et al., 2019). It doesn't have a moon, unfortunately.

Shape There are light-curve shape models for (20) Massalia, such as the model in DAMIT (Ďurech et al. (2018)). However, the DAMIT model (Fig. 3.1) is only preliminary; it shows a convex hull, with a lack of major topography.

Recently, a brand new AO observation of (20) Massalia was made, from which a new detailed shape model was developed (Marsset, pers. comm.). This new model (Fig. 3.2) shows (20) Massalia having a deep depression on one side and a high peak on the other. This most likely relates to a crater and an antipodal peak.

3.2 The Massalia Family

The family itself is compact and well defined. There are more than 18,000 observed asteroids linked to (20) Massalia, as its family members (using a cut-off velocity of $v_{\mathrm{cut}} = 26\,\mathrm{m/s}$). The largest fragment is only 4.9 km in diameter, making it around ∼0.005% of the volume of the largest remnant, which is 131.56 km in diameter.

The cumulative SFD of the family (Fig. 3.3) is steep for multikilometer sizes. The slope between 2 and 5 km is steep, -5.3 ± 0.1. There is a bend in the SFD under the 2 km sizes, and the slope between 2-km and 600 m is shallower,

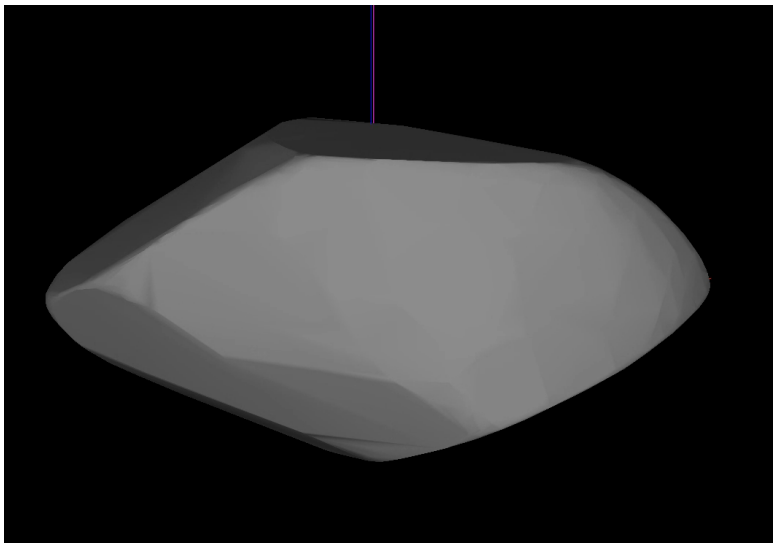

Figure 3.1 Light-curve model of (20) Massalia from DAMIT (Ďurech et al. (2018))

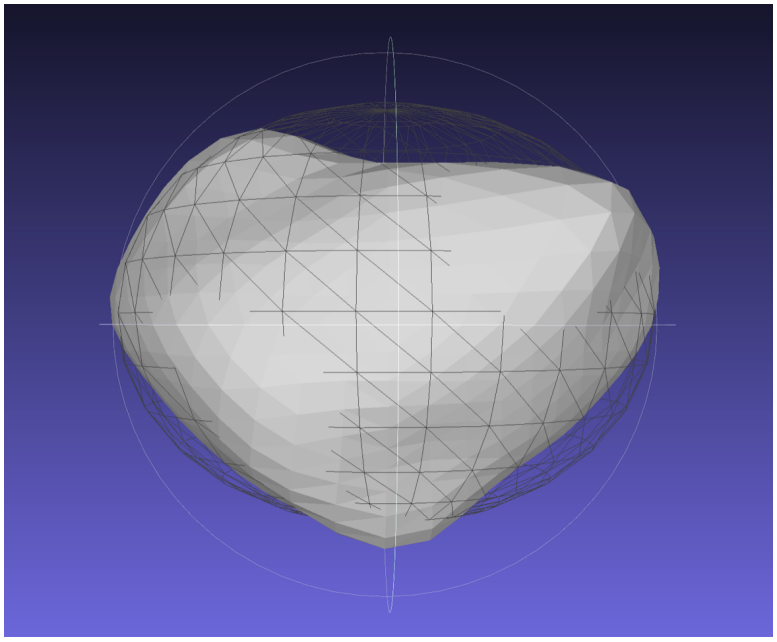

Figure 3.2 Adaptive-optics shape model of (20) Massalia from Marsset (pers. comm.).

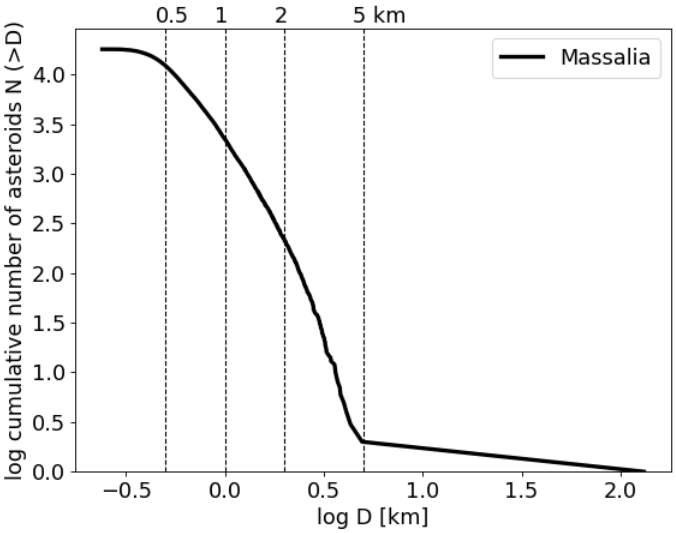

Figure 3.3 Observed cumulative SFD $N(> D)$ of the Massalia family. It is very steep between 2 and 5 km (with a power law slope -5.3 ± 0.1) , but becomes more shallow bellow 2 km (-3.1 ± 0.1). Bellow 500-m, the SFD is flat due to the observational bias.

-3.1 ± 0.1. Such SFDs are typical for relatively young families (Brož et al., 2024). In fact, according to the collisional evolution model from Marsset et al. (2024), the age of the family is 450 ± 50 million years, with another collision about 40 My ago. The observed SFD becomes very shallow at the top, from around 500 m to 200 m. This is due to the observational limit.

The family is spread over more than 0.15 au ($a = 2.32 - 2.47$ au) and is affected by multiple orbital resonances. The strongest mean-motion resonance that directly affects the family is with Mars 1:2 at $a = 2.419$ au. This resonance is likely the main perturber, sending kilometre-sized bodies to the NEO space. There is also the much stronger 3:1 resonance with Jupiter located further behind the family ($a \sim 2.50$ au) and the secular ν_6 ($a \sim 2.1$ au), to which the bodies could travel via the Yarkovsky drift and then be scattered. Proper orbital elements of the Massalia family are shown in Fig. 3.4, together with the relevant resonances.

3.3 Massalia as the Source of L-chondrites

According to Marsset et al. (2024), the Massalia asteroid family is the primary source of L-chondrite meteorites. Additionally, they provide evidence that two impacts struck (20) Massalia and formed two overlapping families.

Studies of fossil meteorites in the mid-Ordovician limestones (466 My old) indicate that the Earth suffered a massive infall of ordinary L-chondrites (Heck et al., 2017; Schmitz et al., 2019; Zhang et al., 2024). They are believed to originate from a single parent asteroid. Nearly half of them are heavily shocked and have distinct radiometric ages $^{40}\mathrm{Ar}/^{39}\mathrm{Ar}$ near 470 My (Swindle et al., 2014). This means an L-chondrite-like asteroid suffered a supersonic impact ~ 470 My ago.

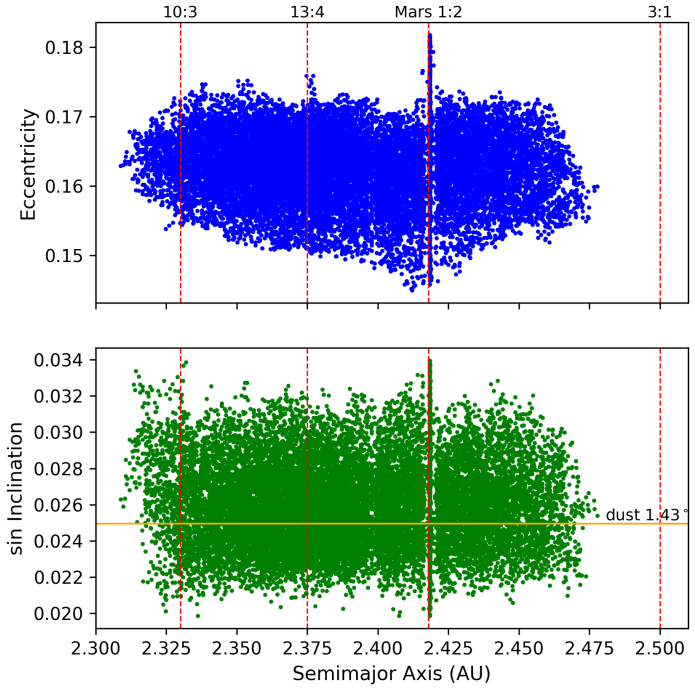

Figure 3.4 Massalia family in proper elements, the semi-major axis vs the eccentricity and the inclination. The mean-motion resonances 3:1, 10:3, 13:4 with Jupiter and 1:2 with Mars are highlighted. The IRAS dust band at 1.43° degree inclination is likely tied to Massalia (Nesvorný et al., 2006).

Marsset et al. (2024) performed a spectroscopic analysis of all major S-type asteroid families in the Main Belt. The only families showing similar composition, pyroxene to olivine ratios, to ordinary L-chondrites are Massalia, Gefion and partly Juno. They follow up with models of collisional evolution; their best-fit age for the Massalia family is 450 ± 50 My, matching the age of the Ordovician meteorites. Additionally, the Massalia family is located between the two most effective pathways to the near-Earth space, the 3:1 mean-motion resonance with Jupiter and the ν_6 secular resonance.

They did the same analysis for the Gefion family, which has an estimated age of 1500 ± 200 My, a very shallow SFD, and its location near the 5:2 resonance reinforces its negligible contributions to the meteorites and NEO population.

Their collisional models also show that Massalia formed a second family about 40 My ago. In fact, Massalia suffering two impacts is the only solution explaining both the shock ages (470 My) and the relatively steep SFD compared to shallow SFDs of old families. This event was tied to the IRAS 1.4° dust band (Nesvorný et al., 2006) and is directly supported by the cosmic ray exposure ages (Graf & Marti, 1995) of contemporary ordinary L-chondrites, which have a minor increase at 40 My.

4 First Impact Simulations

Our goal is to investigate the origin of the Massalia asteroid family. We did so by modeling impact scenarios involving (20) Massalia using the OpenSPH code made by Ševeček (2021). (20) Massalia is suspected to have suffered two impacts (Marsset et al., 2024). Here we focus on modeling the first of the two impacts.

Our first step is constraining the impact energy that could reproduce the observed characteristics of the Massalia family. We started by performing a plethora of low-resolution simulations, varying the size of the projectile while keeping other parameters fixed. For each setup, we computed the synthetic size-frequency distribution (SFD) of the resulting fragments and compared it to the observed SFD of the Massalia family.

We focused on two primary matching criteria:

- The slope of the SFD in the multi-kilometre range, which is observed to be approximately -5.3.

- The size ratio between the largest remnant and the largest fragment, with observed diameters of 131.5 km and 5 km, respectively.

4.1 Simulation Parameters

We have chosen the material parameters to match the (20) Massalia asteroid, as introduced in Section 3.1. Massalia belongs to the L-chondrite-like asteroids. A standard analog used in impact simulations is basalt, so we base most of our material parameters on it. We set the material density to 2700 kg/m^3, which is the estimated density of (20) Massalia and also a typical value for basalt. The specific internal energy was initialized at 1000 J/kg, representing a relatively cold, undisturbed target.

As for the rheological model, we used the Drucker Prager yield criterion (Jutzi et al., 2015). We chose it instead of the simpler von Mises criterion. This choice allows us to model a non-spherical deformation of the body under strong self-gravity. The values of the moduli in the Drucker Prager model were set according to typical values for basalt.

For the equation of state (EOS), we employed the Tillotson formulation introduced in Section 2 The Tillotson parameters are taken from material calibration on basalt in Benz & Asphaug (1999).

Fragmentation is modeled using the scalar Grady–Kipp approach (Grady & Kipp, 1980), a standard method for brittle failure in geological materials. The Weibull exponent (Weibull, 1939) was set to 9, and the Weibull coefficient to 4.0×10^{35}, reflecting a distribution of micro flaws in basalt, as in Benz & Asphaug (1995).

Parameter	**Value**
General properties	
Density ρ	2700 kg/m^3
Specific energy U	1000 J/kg
Rheology: Drucker–Prager	
Bulk modulus K	2.67×10^{10} Pa
Shear modulus G	2.27×10^{10} Pa
Elastic modulus E	8.0×10^{9} Pa
Melting energy	3.4×10^{6} J/kg
Internal friction coefficient	2
Cohesion	9.0×10^{7} Pa
Dry friction coefficient	0.8
Equation of state: Tillotson	
Parameter a	0.5
Parameter b	1.5
Parameter B	2.67×10^{10} Pa
Parameter α	5
Parameter β	5
Incipient vaporisation energy U_{iv}	4.72×10^{6} J/kg
Complete vaporisation energy U_{cv}	1.82×10^{7} J/kg
Sublimation energy U_{sub}	4.87×10^{8} J/kg
Fragmentation model: Grady–Kipp, scalar	
Weibull exponent m	9
Weibull coefficient k	4.0×10^{35}

Table 4.1 Material parameters used in our SPH simulations.

We use the described material for both the target and the projectile. However, the projectile is usually entirely shattered and partially vaporized during the impact. This makes its precise material parameters of minor importance. The dominant factor, on the other hand, is its kinetic energy.

Both the target and the projectile were initialized as spheres. The target body had a diameter of 134 km, slightly larger than the observed diameter of (20) Massalia. We were using the SPH method; therefore, we discretized the sphere into particles. Our resolutions ranged from 100,000 to 3.2 million particles, in the case of our highest-resolution simulations.

The impact velocity was set to 5 km/s, which corresponds to the mean impact velocity in the main asteroid belt (Dahlgren, 1998).

There was a short stabilization period of 500 s before the impact itself. We included this phase to dampen initial particle velocities and to allow the system to reach equilibrium. An even shorter duration would suffice, since a sound wave traverses the body in only about 45 seconds, but the stabilization is computationally inexpensive. Nevertheless, we chose a longer duration to ensure proper relaxation after observing some issues with incomplete damping.

The fragmentation phase, which included the impact itself along with subsequent fragmentation and early reaccumulation, typically spans 5 hours. That is enough time to capture the most dynamically sensitive phase of the impact. It is also the most computationally demanding part of the simulation, scaling as $\mathcal{O}(N \log N)$, where N is the number of particles.

Following fragmentation, a hand-off procedure of SPH particles into rigid spheres for an N-body reaccumulation. This phase lasted approximately 11.5 days (or 10^6 s) and allowed the whole system to settle down.

4.2 Simulation Overview

The following description outlines the evolution of the impact event as observed in our simulations. Key moments are illustrated by snapshots shown in Figs. 4.1 and 4.2, capturing the progression from the beginning of the impact until the largest remnant acquires its final shape.

Shock In the first seconds of the simulation, the high-velocity projectile struck the surface of the target body. Right after the impact, the projectile compressed both itself and the surrounding material, reaching pressures up to P = 50 GPa. The kinetic energy released in the collision was equivalent to $17 \cdot 10^6$ megatons of TNT. The heat generated during impact resulted in the partial vaporization of both the projectile and the surrounding material. An expansion followed, ejecting material from the target. An intense shock wave was launched from the impact point, propagating through the entire target at approximately 5 km/s—significantly faster than the respective sound speed of 3 km/s. Within just 27 seconds, the shock front traversed the full diameter of the target.

Fracture This energy transmission initiated widespread fracturing and pulverization of the target, reducing it to a gravitationally bound rubble pile, with little to no internal cohesion. The severity of the disruption excludes the event from being classified as cratering. Even though the largest remnant was similar in size to the original body after reaccumulation, the impact should be classified as catastrophic.

Ejection Consequently, material from the vicinity of the impact point was ejected outward, forming an ejecta curtain mostly in the impact plane, perpendicular to the surface normal at the point of contact. A slow-moving, gravitationally bound core of the target remained, while the outer surface layers began to break away. The ejecta consisted primarily of single particles, with occasional small clumps. Larger fragments tended to originate from a 45th-degree angle from the impact, near the boundary between the impact point ejecta and surface layer debris.

Reaccumulation The impact energy was insufficient to fully eject the entire surface layer; roughly half of the ejected material was reaccreted quickly (within minutes). The escaping portion, opposite to the projectile's velocity, expanded outward in a loose form of stream, spanning roughly from the impact point to the antipodal point. However, it was still bound and subsequently formed a "tail" and reaccreted. This tail material gradually settled back onto the far side of the core, contributing to the peak at the antipode. The ejecta curtain traveling substantially faster than the core ($v_{curtain} \sim 50$ m/s, $v_{core} \sim 5$ m/s) overtook it and also reaccreted onto the surface.

Late Stages About two hours after impact, the ejecta curtain reached the antipode. However, the reaccumulation at the antipode was dominated by the returning tail, which eventually built up into a distinct peak. Meanwhile, fragments with sufficient velocity to escape the gravitational influence of the core continued to disperse outward ($v_{ecs} = 80$ m/s). Due to gravity, larger fragments reaccumulated in the dispersed material, forming new asteroids and, with them, a collisional family.

4.3 Impacts into Monolithic Body

From the low-resolution simulations, we obtained the best agreement with observations for impact energy of $Q/Q^* \approx 0.1$, where Q^* is the critical disruption energy derived from the scaling law of Benz & Asphaug (1999). Fig. 4.3 shows SFDs multiple low resolution ($4 \cdot 10^5$ particle) simulations with varying projectile sizes and angles.

We then focused on the most promising impacts, specifically a 16- or 20-km projectile hitting the 134 km main body at 5 km/s and at 45-degree angle.

In the first set of simulations, the main body itself was assumed to be a monolith. The cases with different internal structures, such as a rubble pile, will be discussed later.

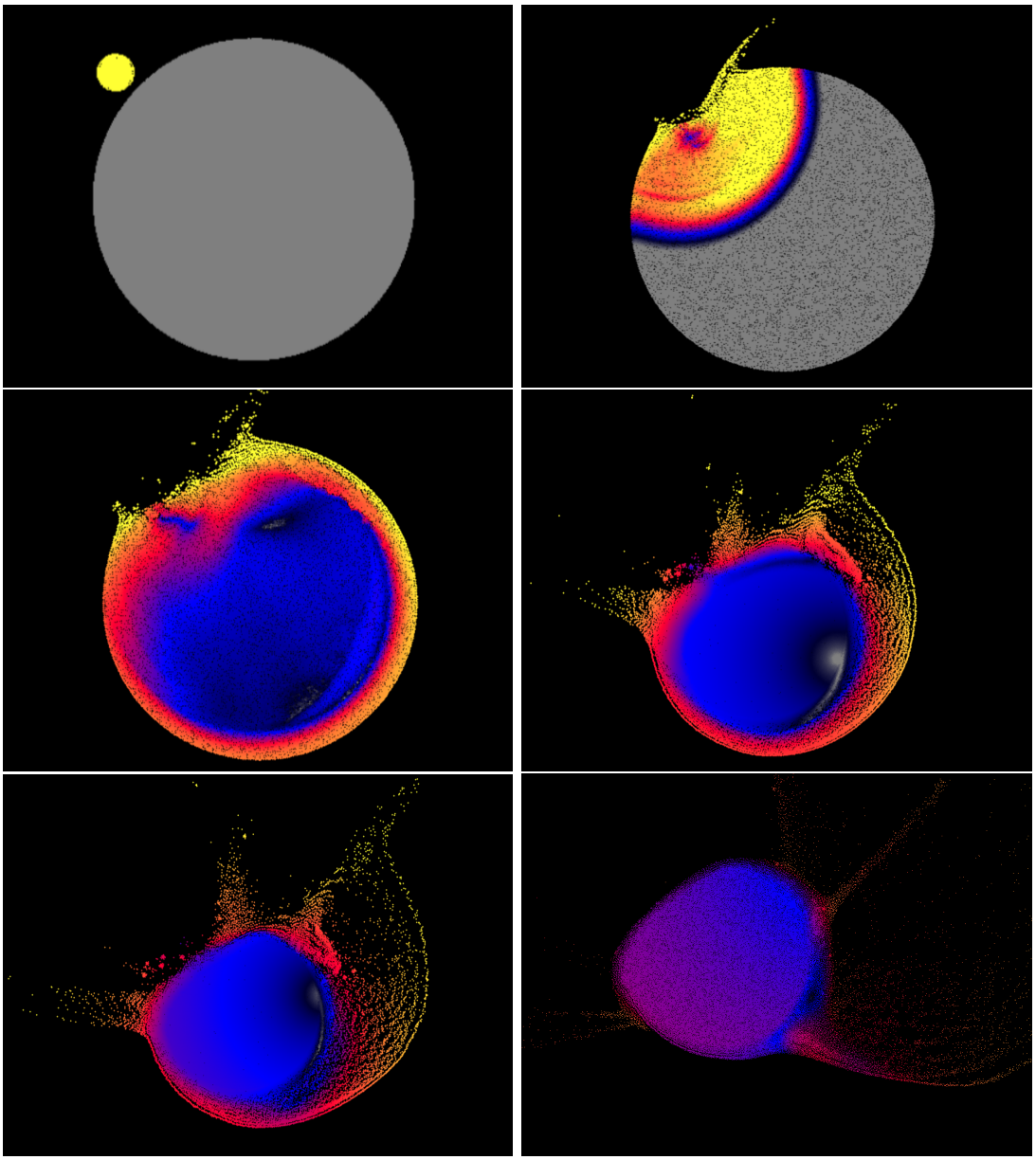

Figure 4.1 Snapshots from our simulation of a 16-km projectile striking a monolithic, 134-km target. The individual snapshots represent a planar cross-section in the xy-plane, taken at the simulation time of 0 s, 10 s, 100 s, 7.5 min, 15 min, and 45 min. Particle velocities relative to the original body's rest frame are shown on a color scale, with blue indicating 1 m/s, red 20 km/s, and yellow 100 m/s. The first two frames capture the initial impact, including the destruction of the projectile and the propagation of the shock wave. By the 100th second (third frame), the shock wave has traversed the entire body, leaving it fully fragmented and damaged. The outer surface layers are clearly accelerated compared to the inner core. The fourth and fifth frames highlight the two dominant sources of ejecta: the impact point and the surface layer. Distinct particle clusters form near the transition between these zones, likely giving rise to the largest fragments. The final frame (45 min) shows the ejecta curtain overtaking the main body and the formation of a reaccreting "tail" trailing behind, originating from the ejected surface material.

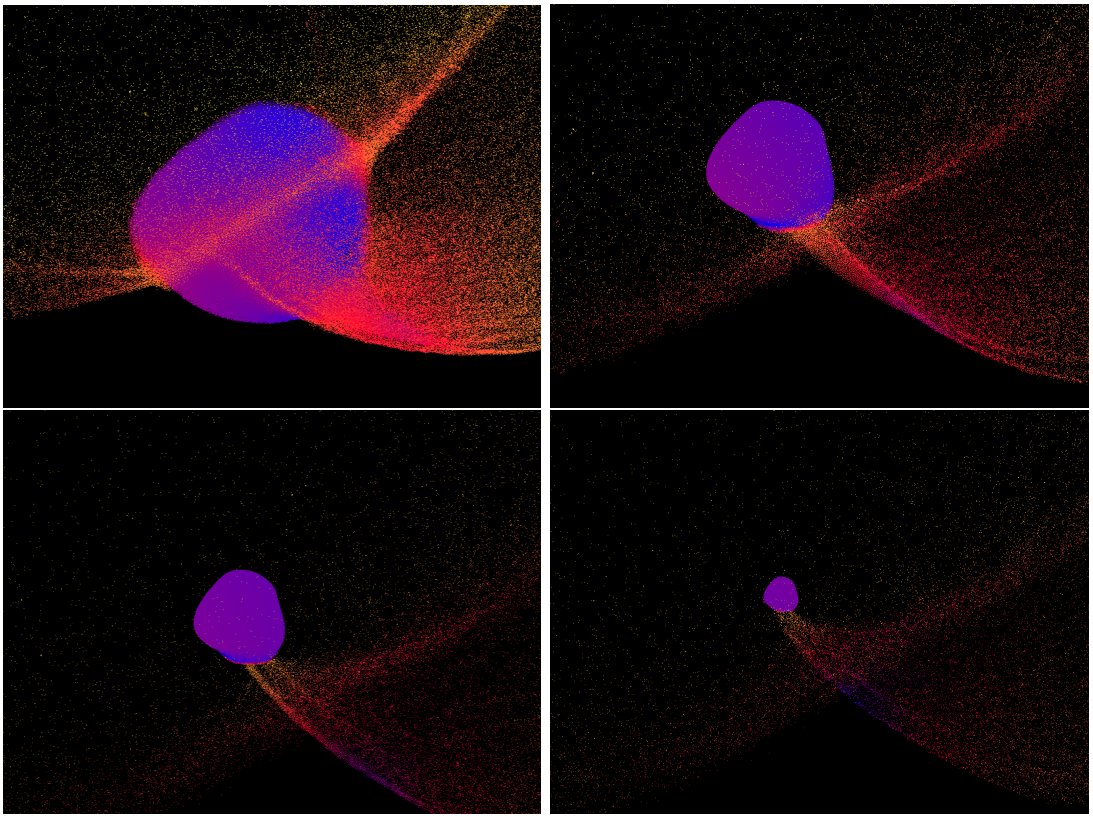

Figure 4.2 Same as Fig. 4.1, but for later snapshots showing also the broader surrounding. The snapshots were taken at 45 min, 2 h, 5 h, and 12 h after the impact. The first frame again shows the ejecta curtain advancing past the core and the ejected surface material beginning to reaccrete at the antipodal region. By 2 h, the ejecta curtain reaches the antipode. From that point onward, reaccretion occurs primarily at the antipode, forming a single peak. The rest of the ejecta either reaccretes more slowly or escapes, contributing to the formation of the asteroid family.

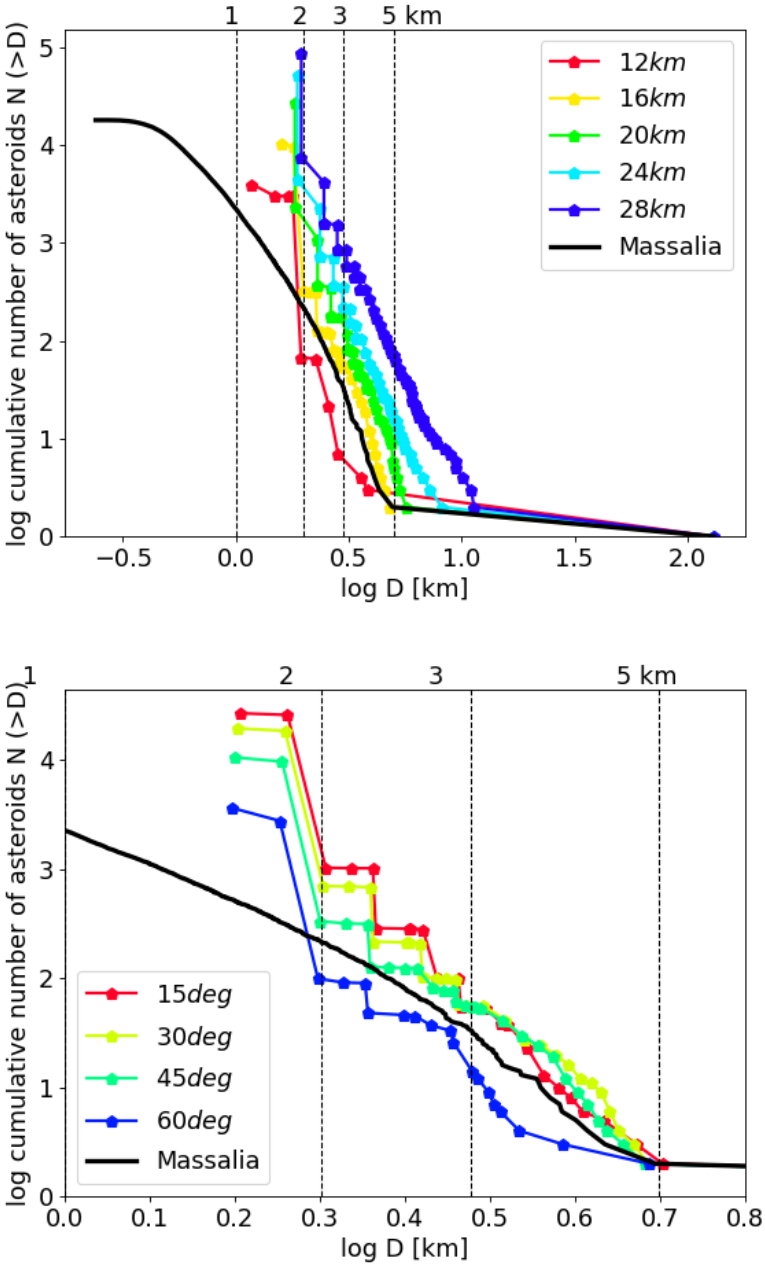

Figure 4.3 Synthetic SFDs from low resolution simulations with varying impact projectiles (top) and impact angles (bottom) for 16-km projectiles, all hitting 134-km monolithic body.

4.3.1 Low vs High Resolution

In SPH simulations, numerical resolution plays a crucial role in the accuracy and reliability of the results. One of the key challenges encountered in this study is the limited resolution of simulations. At low resolutions, individual SPH particles represent large volumes of material. In the case of a 100,000-particle simulation, each particle corresponds to a body roughly 2.9 km in diameter. This restricts the simulation's ability to resolve small-scale structures and fragmentation processes, effectively limiting the synthetic SFD to multi-kilometre bodies only. By increasing the number of SPH particles, we can significantly improve the resolution. In our highest-resolution run with 3.2 million particles, the smallest particles reached the scale of approximately 0.9 km. However, the computational cost rises with resolution, requiring substantially more runtime and memory. We ran the simulations at the university's HPC, chimera. Our simulations ran on 64 CPUs and the computation time rose from a few hours in the low-resolution cases up to 2 weeks.

We performed simulations with different resolutions, with 1, 2, 4, 8, 16 and 32 $\times 10^5$ particles. We were interested in the stability of the SFD. As resolution increases, the SFD systematically shifts to the left, indicating a smaller number of large fragments relative to those in lower-resolution models. This effect is particularly evident when comparing cumulative SFD curves across different resolutions (see Fig. 4.4). The shift appears to stabilize just above the 3.2 million particle threshold, suggesting that we achieved convergence at this resolution or just above it.

Moreover, lower-energy collisions tend to fragment the target less violently, resulting in slower convergence in the SFD. In our case, the specific impact energy Q corresponded to approximately $\approx$0.1 Q*, which contributed to the slower convergence behavior.

Additionally, some effects cannot occur when all particles are several kilometers in size. For example, surface layer ejection, which is visible in high-resolution simulations, is not reproduced in low-resolution ones due to the particle size. This effect is illustrated in a comparison of original particle positions for two resolutions in Fig. 4.5.

4.3.2 Impact with 16-km Projectile

Let us now examine the synthetic SFD from a 16-km projectile impact at the highest resolution and compare it to the observed SFD of the Massalia family. The distributions are plotted in Fig. 4.4

The synthetic distribution agrees well with observations in the multi-kilometer range. The two largest simulated fragments are 4.78-km in diameter, compared to Massalia's 4.9- and 4.3-km. Between 5 km and 3 km, the slope is -5.1 ± 0.2, matching that of the observed family.

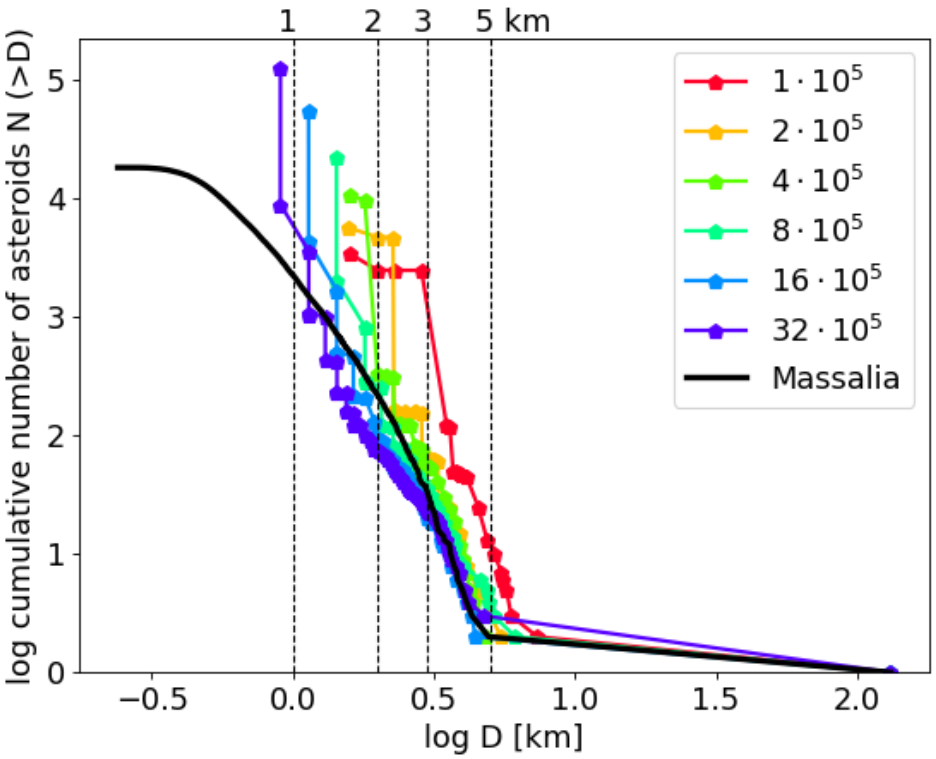

Figure 4.4 Synthetic size-frequency distributions of variously crude simulations. The impacts are of 16 km projectiles hitting a monolithic 134 km spherical body. The observed Massalia family is in Black. There are systematic shifts towards smaller sizes with growing resolutions. The size shift between cases with twice the particles is from 20 %, decreasing to less than 1 % for the last two resolutions. The slope for the most detailed simulation is steep and matches the observed distribution until 3 km; after that, it becomes too shallow. The last few points on each distribution are single-particle fragments, a relict of the resolution.

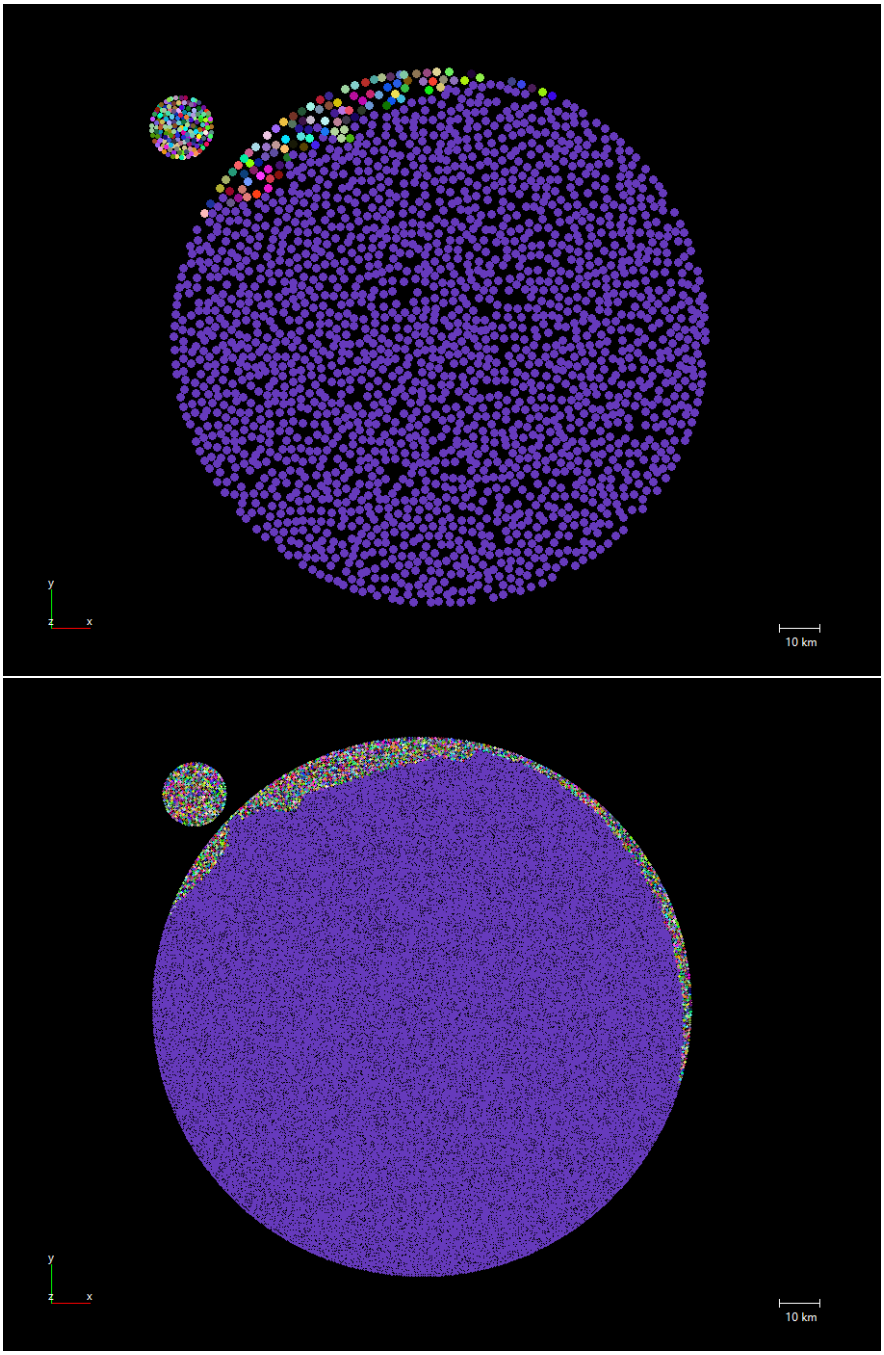

Figure 4.5 Original positions of ejected particles in our simulations, using 2×10^5 (top) and 3.2×10^6 particles (bottom), respectively. All parameters were identical except for the resolution. Each final fragment is rendered using a unique color, and most particles remain as part of the largest remnant. Both simulations show substantial ejection from the impact point, but only the high-resolution simulation resolves the ejection of a $\sim$2 km-thick surface layer extendnig almost upto the anitpode.

However, below 3 km, the synthetic distribution becomes noticeably shallower, with a slope of -3 ± 0.1. This inflection point occurs earlier than in the observed distribution, where a similar change in slope appears closer to 2 km.

At sizes around 1 km, the synthetic number of fragments increases sharply, exceeding observed counts. This is a resolution artifact: the simulation approaches its lower size limit, defined by the smallest SPH particle, which is ≈0.9 km.

It is worth noting that the steep portion of the SFD in the multi-kilometer range is stable over long timescales, because the collisional evolution is relatively slow. In contrast, the sub-kilometer range tends to evolve, becoming shallower over millions of years due to collisional grinding and dynamical decay. This evolution brings the respective slope closer to the average slope of the background, main-belt population.

Ejected Volume and Ejecta Sources The total volume in the 16 km impact simulation was approximately 50,000 km^3, or just under 4% of the total pre-impact volume (1,250,000 km^3).

As shown in Fig. 4.5, the ejecta originated from two distinct regions. Roughly 40% of the ejected material came from the vicinity of the impact point. This material formed an ejecta curtain, most of which reaccreted onto the surface of the main body or nearby regions.

The remaining 60% originated from a thin surface layer, approximately 1-2 km thick. This material was stripped off during the early stages of the impact, forming a coherent ejecta tail that partially reaccreted at the antipodal point.

This surface-layer ejection only became apparent at higher resolutions when SPH particle sizes are small enough to resolve the thin layer. Notably, around 33 of the 50 largest fragments originated from this surface layer, underscoring its significance in the production of fragments.

The Largest Remnant Thanks to the use of the Drucker Prager criterion (Jutzi et al., 2015), the largest remnant exhibited a nontrivial shape, shown in Fig. 4.6. The entire target body was fully damaged and fragmented to a gravitationally bound pile of rubble. Despite this, the remnant retained around 96% of its original mass, due to self-gravity. Its final shape was nearly spherical, with only minor deviations. The axial ratios, $c/b = 0.98$ and $b/a = 0.97$, indicate a slight flattening and elongation. The two most prominent deformations included a flattened plateau at the original impact point and a reaccreted bulge at the antipode, formed by the fallback of material from the ejecta tail.

Rotation We assumed no initial rotation prior to impact, and the collision did not impart significant angular momentum to the remnant. As a result, the final body rotates with a period of $P = 4.7\,\text{days}$. For comparison, the critical period for a body with density $\rho = 2700\,\text{kg/m}^3$ is $P_{\text{crit}} = 1.4\,\text{h}$ and the observed period of (20) Massalia is $P_{\text{crit}} = 8\,\text{h}$ (Cellino et al., 2019).

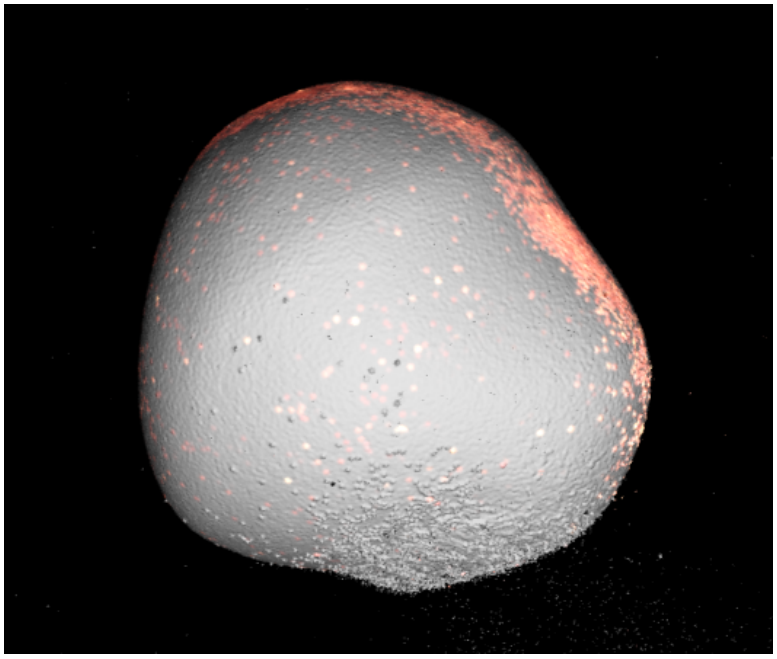

Figure 4.6 The final shape of the largest remnant from simulation of impact with 16 km projectile. It is flattened around the point of impact and a has a bulge near the antipode

Velocity of Fragments We also computed the distribution of fragment velocities, analogous to the size-frequency distribution (Fig. 4.7. The histogram shows the number of fragments as a function of their absolute velocity $|\mathbf{v} - \mathbf{v_l r}|$, measured relative to the largest remnant. The peak in the velocity distribution in the simulation is approximately $\mathrm{v} = 50\,\mathrm{m\,s^{-1}}$, which is lower than the escape velocity. The escape velocity from a $\mathrm{D} = 134\,\mathrm{km}$ body is $\mathrm{v_{esc}} = 80\,\mathrm{m\,s^{-1}}$. This suggests that the resulting asteroid family should remain relatively compact, with most fragments staying in the vicinity of the parent body. The velocity distribution is relatively narrow, reflecting the low-energy nature of the impact.

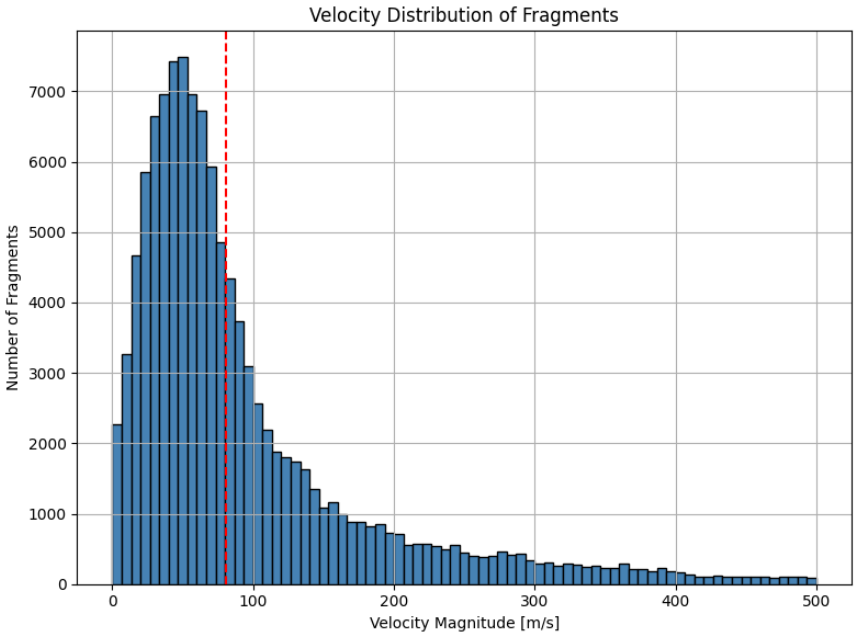

Figure 4.7 Differential histogram of fragment velocities, computed with respect to the largest remnant. The simulated impact involves a 16-km projectile. The escape velocity from such body is $v_{\text{esc}} = 80\,\text{m/s}$, highlighted in red.

4.3.3 Impact with 20-km Projectile

The second impact we explored in detail was the 20-km impactor. We compare the results of this simulation with those of the slightly less energetic case, discussed in Section 4.3.2.

Ejection and Reaccretion The increase in impact energy was immediately noticeable, with the specific energy rising from $Q/Q^* \sim 1\%$ to $Q/Q^* \sim 1.5\%$. This increase led to slightly different fragmentation behavior. Snapshots taken 15 minutes after impact, shown in Fig. 4.8, reveal not only a more extensive ejection from the impact point but also widespread surface ejection across the entire body, rather than being limited to one side from the impact point to the antipode as before.

In addition, several large fragments broke off around the 45° angle from the impact point. These fragments partially reaccreted, forming a secondary slowly reaccreting tail. This region remained the primary source of multi-kilometer fragments. Overall, the total ejected volume corresponded to over 9% of the pre-impact volume.

SFD The synthetic SFD is shown in Fig. 4.9. The highest-resolution simulation, using 3.2×10^6 particles, produced a distribution that closely matches the observed Massalia family, except for the three largest fragments. The largest synthetic fragment had a diameter of 6.5 km—about 1.5 km larger than the largest observed fragment. Beyond these outliers, the SFD aligns well with observations, matching the slope of -5.2 ± 0.1 down to 1.5 km, which is near the resolution limit of the simulation. At this size range, there is also a slight bend in the observed

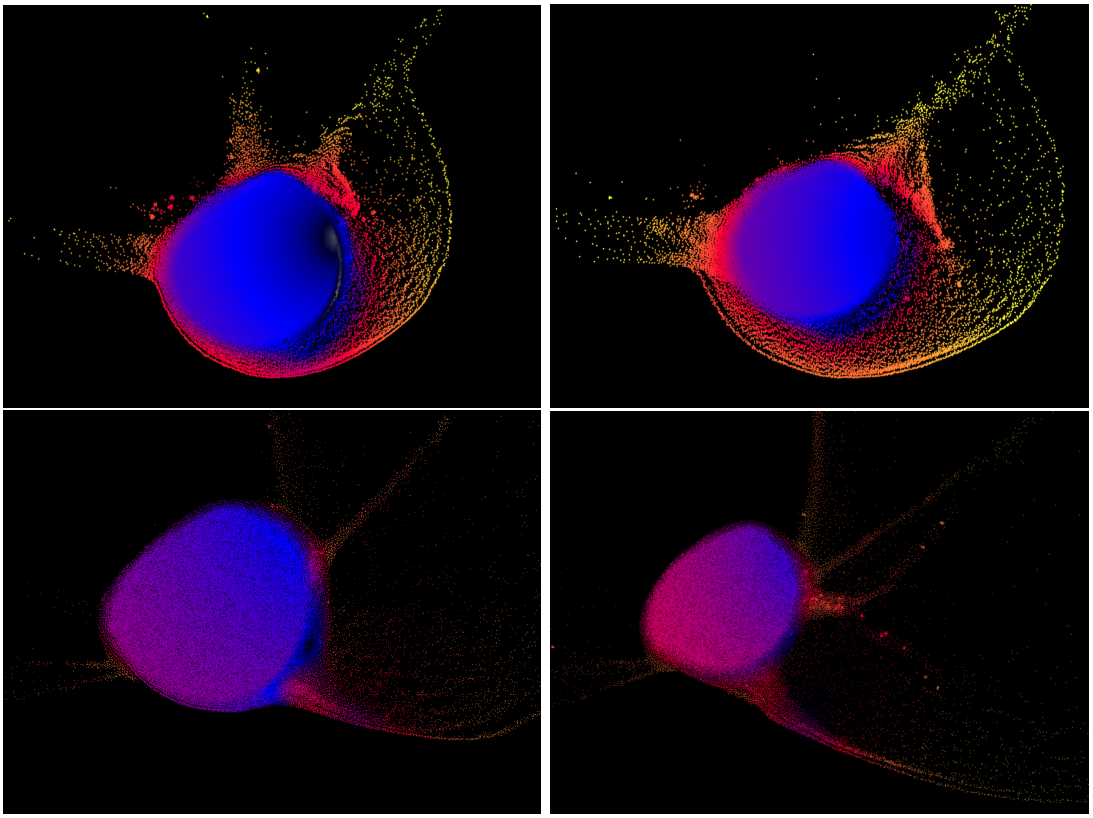

Figure 4.8 Comparison of impacts with 16-km (left) and 20-km (right) projectiles, shown at 15 min (top) and 45 min (bottom) after impact. The more energetic 20 km impact produces widespread surface ejection and large fragments breaking off near the 45° angle from the impact point. Some of these fragments partially reaccrete, forming a secondary ejecta tail.

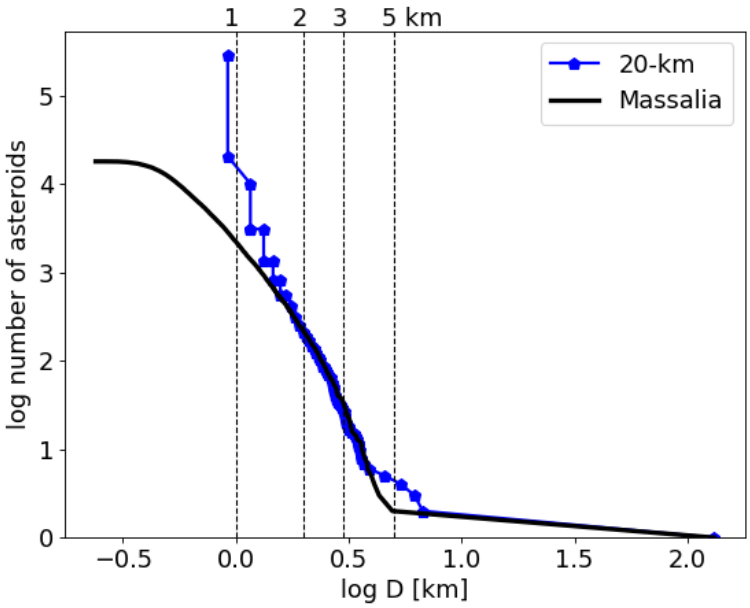

Figure 4.9 Same as Fig. 4.4 for the impact with 20 km projectile, compared to the observed Massalia family. While three fragments are significantly larger than their observed counterparts, the remainder of the distribution closely follows the Massalia family down to 1.5 km. The spike at 1 km is again due to limited resolution.

distribution, which we are unable to reproduce due to the resolution limit. In Marsset et al. (2024), the part below 1.5 km was extrapolated down to dust sizes.

Final Shape The final shape of the largest remnant was noticeably flattened on the impact side. The most prominent new feature, compared to the previous simulation, is the relatively larger reaccreted bulge forming at the antipode. The measured axial ratios are $c/b = 0.98$ and $b/a = 0.81$, indicating the distortion caused by antipodal reaccretion.

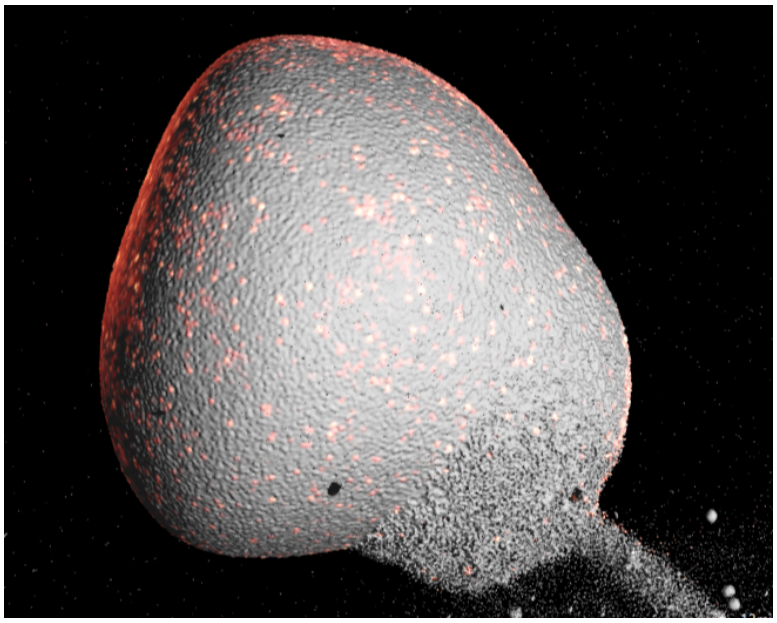

Figure 4.10 The final shape of the largest remnant for impact with a 20 km projectile. The object is no longer spherical, it is flattened at the impact site and has a prominent bulge at the antipode.

5 Second Impact Simulations

There is evidence, as explained in Sec. 3.3, for two impacts on the asteroid (20) Massalia. Acording to simulations discussed in Chapter 4, the first impact was energetic enough to damage the entire body and create a rubble-pile structure. This sets the stage for the second batch of simulations. Hereinafter, we thus assumed a different rheology and performed a second set of simulations, which shall be interpreted as the second impact on (20) Massalia.

5.1 Impacts into a Rubble Pile

Our simulations were set up identically as in Sec. 4.1, with one key difference: the target body was assumed to be already fully damaged prior to the impact. In practical terms, this meant that the damage variable was set to 1 across the entire body, causing the material to behave as granular. In this regime, the yield strength depends only on the pressure and the coefficient of the dry friction.

We again focused on impacts involving 16 km and 20 km projectiles, as these produced the most compelling results compared to higher- or lower-energy impacts.

Simulation Overview There were immediate and noticeable differences between impacts into a rubble pile and into a monolithic body. These differences are illustrated in Figs. 5.1 and 5.2, which show key snapshots and features of the simulations.

The most prominent was the absence of significant surface-layer ejection. Material was only ejected from the immediate vicinity of the impact point. As the projectile struck, it deformed the body by pushing material to the sides from the center rather than excavating a crater.

The ejecta curtain moved ahead of the main body and reaccreted asymmetrically—primarily along the sides and also at the antipode. At the antipode, a steep peak formed, more prominent than in the monolithic case. The antipodal peak was steeper than the bulge created by impacts from Chapter 4, because the reaccretion from just the ejecta curtain is short, focused, and is not overshadowed by the "tail" from surface ejection, which was not present.

Scaling Resolution and SFD Shifts The shift of the SFD towards smaller sizes with increasing resolution was even more pronounced here. Figs. 5.3 and 5.4 show the SFDs for different resolutions for the 16 and 20 km impacts. Between simulations with a twofold increase in particle number, the characteristic fragment sizes shifted by approximately 15%, with the shift diminishing as resolution increases. Although convergence is expected at sufficiently high resolutions, further simulations became computationally too expensive beyond the 3.2 million particle resolution.

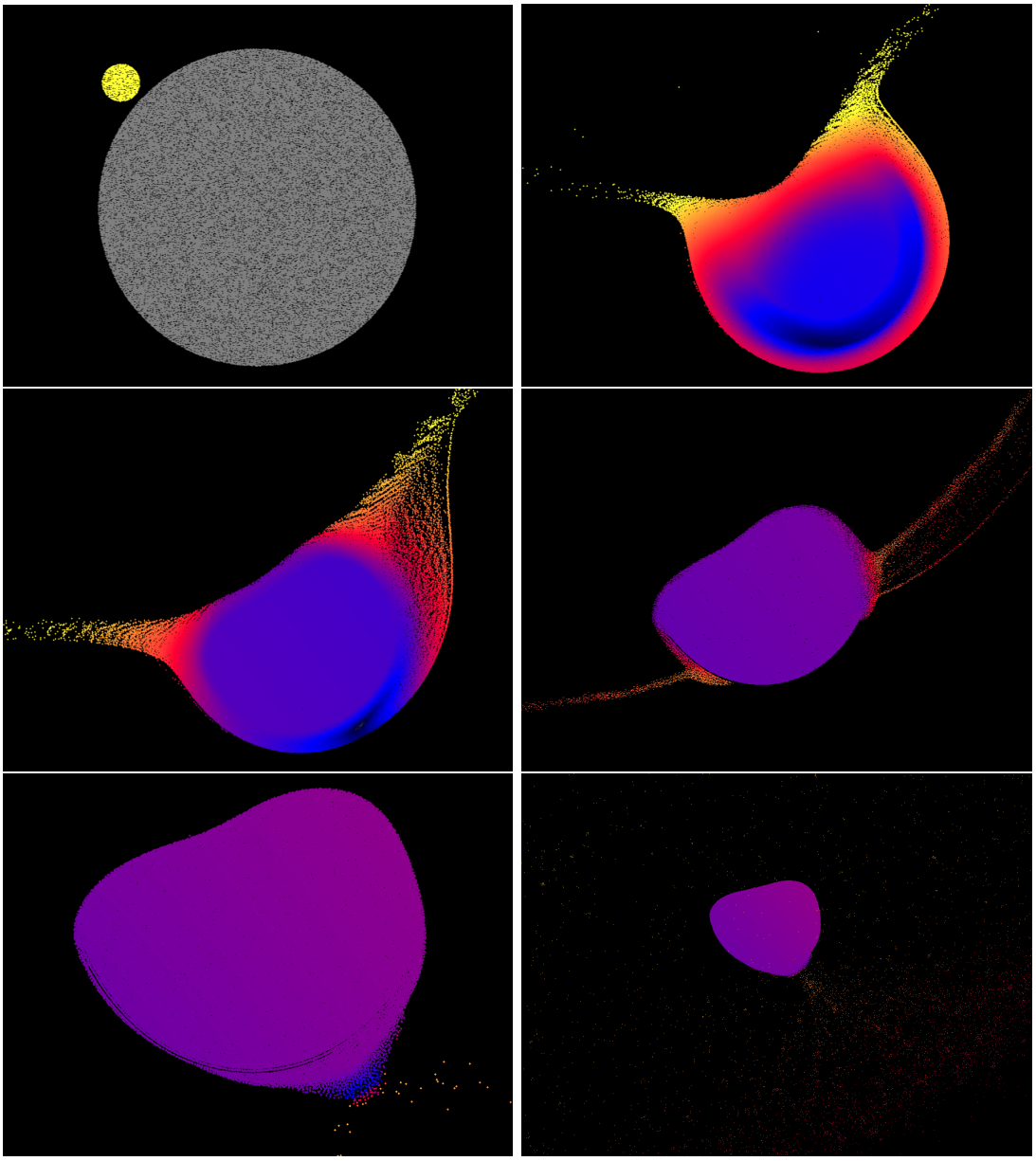

Figure 5.1 Same as Fig. 4.1. with snapshots from the rubble-pile simulation. They were taken at 0 s, 4 min, 15 min, 1 h, 3 h and 5 h after impact. The first shows the initial configuration. The second and third frames capture the deformation of the main body and the ejection of material away from the impact point, forming the ejecta curtain. The fourth frame highlights partial reaccretion onto surface as the ejecta curtain continues to expand beyond the main body. In the fifth snapshot, the ejecta curtain has fully overtaken the remnant, forming a pronounced antipodal peak. After this point, reaccretion slows significantly, and no major structural changes occur.

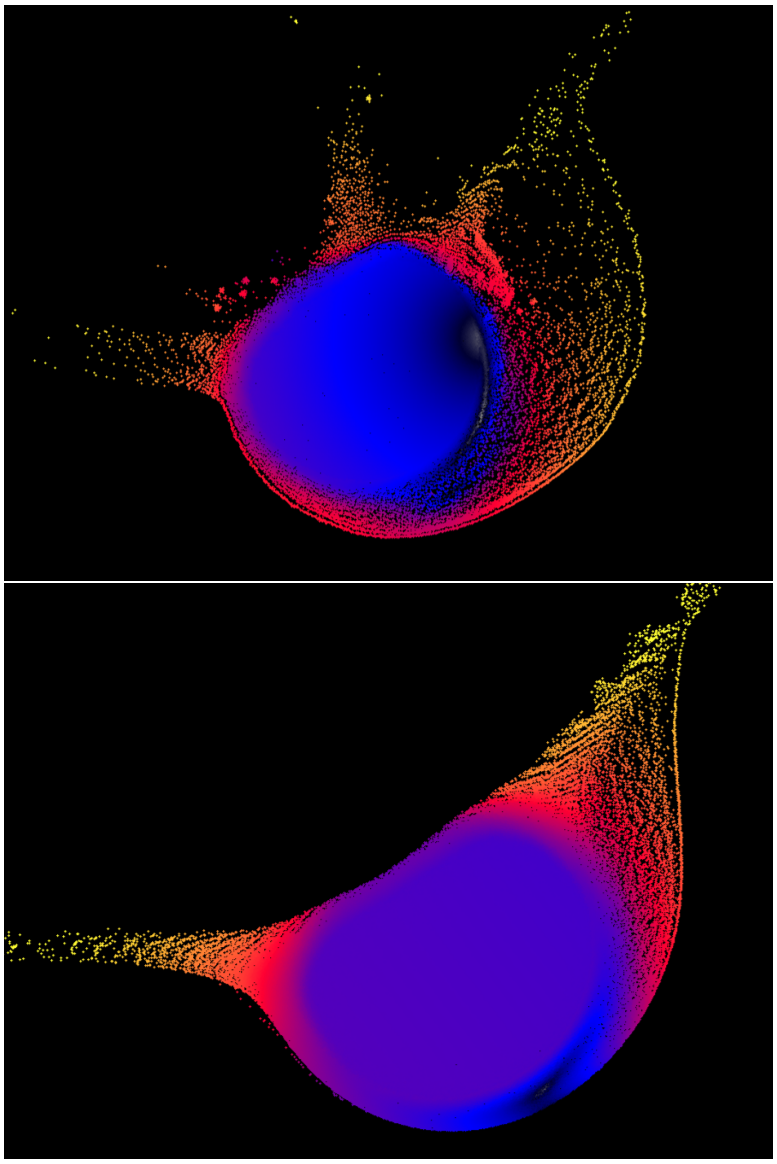

Figure 5.2 Comparison of the impact state 15 minutes after the collision for the monolithic (top) and the rubble-pile (bottom) targets. The rubble-pile body, lacking internal cohesion, undergoes significant deformation, spreading laterally and backing surface-layer ejection. Moreover, there are no distinct clumps of paticles ejected from the impact point. This results in a significantly steeper size-frequency distribution, but having a lower number of multi-kilometer fragments.

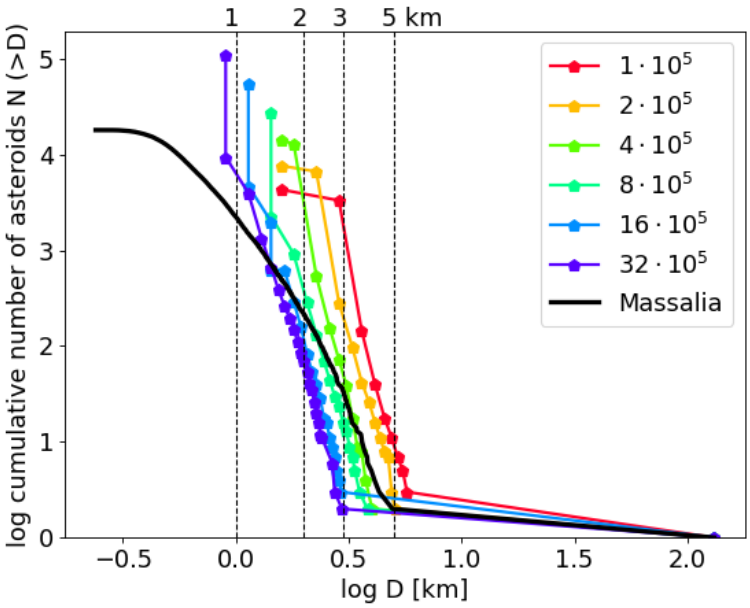

Figure 5.3 Same as Fig. 4.4. Synthetic SFD for rubble-pile impacts. The observed Massalia family is in black. In this case, the shifts between resolutions are approximately 15%. The slopes are very steep, -9.1 ± 0.2, much steeper than those observed in the Massalia family (-5.3 ± 0.2)

Despite the differences in resolution, the ejected volume remained consistent: approximately 3.5% of the original volume for the 16 km projectile and 7% for the 20 km projectile.

The SFD slopes in all simulations were very steep, at -9.1 ± 0.2 and -8.3 ± 0.2 for the 16 km and 20 km cases, respectively. Their largest fragments were 3.0 and 4.1 km. In other words, more small fragments were produced, which turned out to be an advantage when two SFDs (steep and shallow) are combined.

The Largest Remnant The impact significantly altered the shape of the largest remnant (see Fig. 5.5). At the impact point, a broad plateau with a shallow central depression formed — i.e. the location from which nearly all of the ejecta originated. The plateau appears to be sunken by about 20 km when compared to an ellipsoid. However, this deformation is partly due to stretching, as material was pushed laterally during the impact, rather than solely ejected.

At the antipode, a pronounced peak formed as ejecta reaccreted after overtaking the largest remnant. This antipodal structure is sharper and more localized than in the monolithic case.

The axial ratios of the remnant were $c/b = 0.81$, $b/a = 0.99$ for the 16 km projectile and $c/b = 0.76$, $b/a = 0.98$ for the 20 km projectile.

Comparison to Observations We can compare our synthetic largest remnant to the AO observations by (Marsset pers. comms.) in Fig. 3.2. There are many similarities; namely, both bodies have a broad convex plateau or basin on one side;

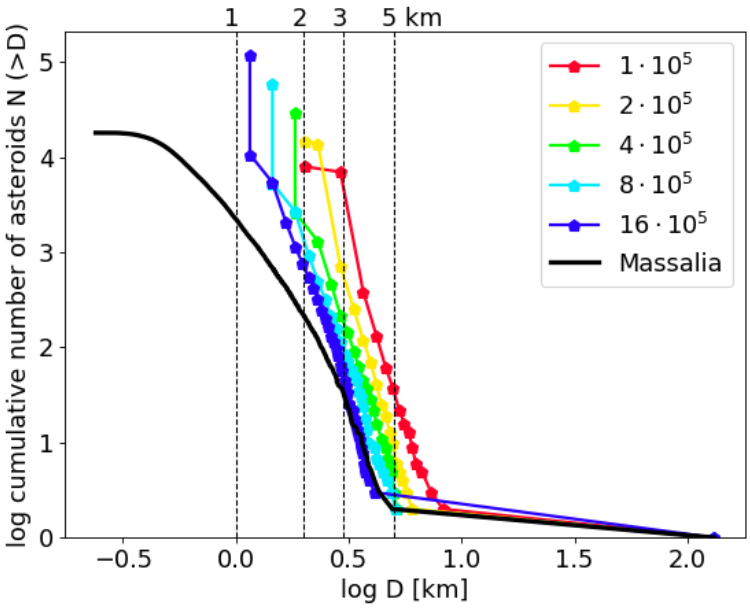

Figure 5.4 Same as Fid. 5.3, but with larger projectile, D = 20 km. The convergence is slightly faster but still out of our resolution limit. The slopes of the distributions are less steep, -8.3 ± 0.2 compared to -9.1 ± 0.2, but still steeper than the Massalia family itself.

this is possibly the impact crater. Both bodies are also deformed to the sides and an antipodal peak. Both have a sort of "heart-like" shape. However, the synthetic shape is slightly rounder.

5.2 Combining Two Impacts

Hereinafter, we combine the first impact to a monolithic body with a second impact to a rubble-pile. In this approach, we neglect millions of years of collisional evolution that would occur between the impacts. This is justified, as such evolution primarily affects sub-kilometre fragments, which lie below our resolution limit. We also assumed a spherical target shape for the second impact. This is also justified because the largest remnant from the first impact was nearly spherical, and the second impact was sufficiently energetic to reconfigure the whole body.

The first impact—a 16-km projectile hitting a 134-km monolithic target—produced a SFD that was insufficient in the 1-3 km range when compared to the observed Massalia family distribution. The second impact helps to compensate for this deficit due to its steep SFD. When we combined both impacts, the resulting size-frequency distribution (Fig. 5.6) matches the observed family better. The combined slope was -5.0 ± 0.1 down to 1.5 km, below which resolution effects become significant.

We can further improve this by slightly increasing the impact energy of the second impact. A small increase of the impact energy in the rubble-pile scenario only shifts the SFD to the right, and the change in slope is negligible. Fig. 5.7

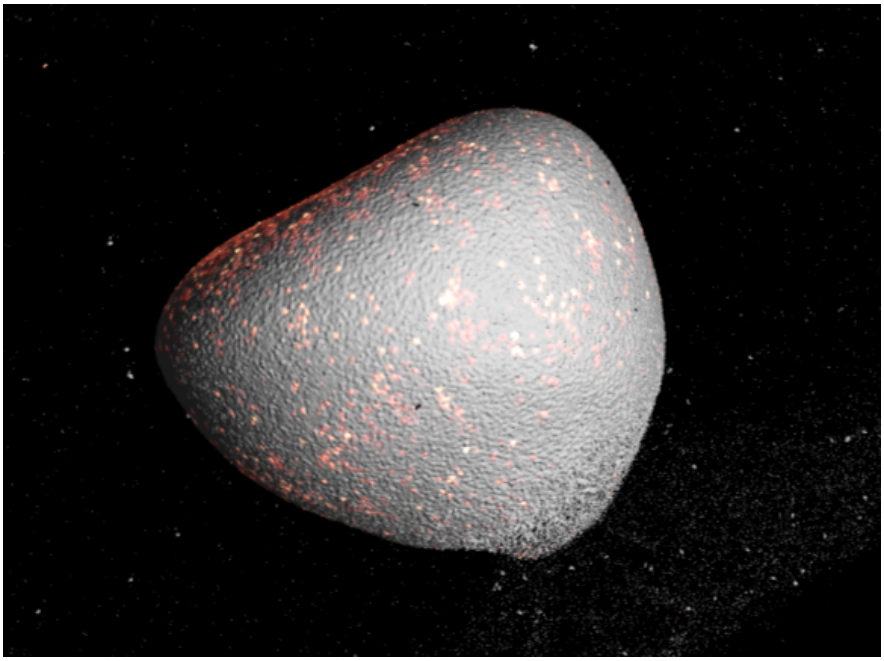

Figure 5.5 The final shape of the largest remnant for the impact with 16 km projectile. It has a broad plateau at the impact side and a prominent peak at the antipode.

shows several SFDs obtained by combining a monolithic impact with a rubble-pile impact shifted by a small amount. This combination allowed us to achieve an even better match than the previous single monolithic impact with a 20-km projectile. By interpolation, we estimate the ideal projectile would be around 18 km in diameter.

In total, the two-impact scenario ejected approximately 7-10% of the parent body's volume, if we only account for multi-kilometer fragments.

5.3 Meteoroid and Dust Production

A real asteroid impact creates fragments of all the different sizes, from multi-kilometre bodies down to micrometer-sized dust grains. Indeed, for the second impact, there is an IRAS dust band observed at 1.4° inclination (Nesvorný et al., 2006), which is aligned with the Massalia family and linked to the family-forming event (Marsset et al., 2024). That implies the dust band, whose population is in the order of 4×10^{23} dust particles, should be a part of the size-frequency distribution. However, our simulations only account for fragments larger than 0.9 km. Hence, we try to extrapolate.

Another anchor we can compare our extrapolation with is the expected number of meter-sized L-chondrites, which is currently 10 to $30 \cdot 10^{10}$, but right after impact should have been around $\sim 1.3 \cdot 10^{13}$.

Our impact models match the observed SFD down to ∼1.5 km (Figs 4.9, 5.6). For these cases, we extrapolated using various slopes from -2.8, which is the slope of the observed family below 2 km, up to -3.3, where the extrapolated volumes become unreasonably large. We also varied the point where we made the

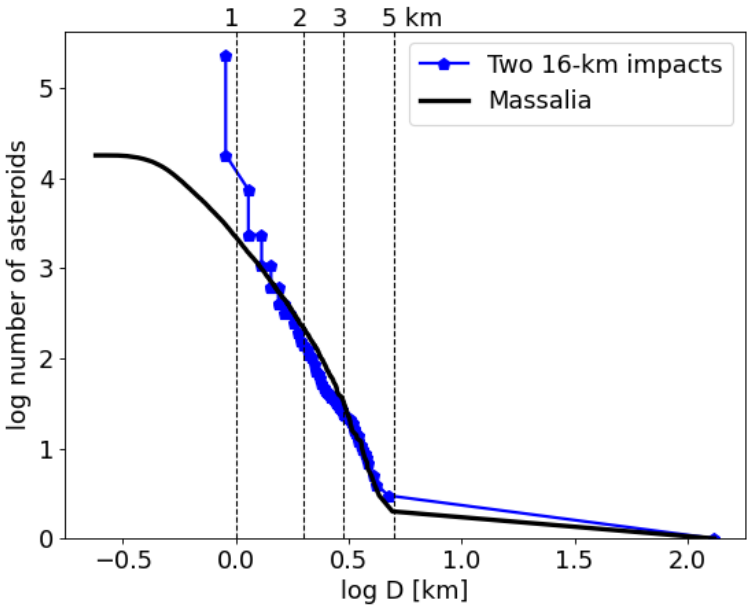

Figure 5.6 Synthetic SFD obtained by combining two impact simulations: a monolithic target and a rubble-pile target, each hit by a 16 km projectile. The resulting SFD matches the observed Massalia family distribution well, down to the sizes of 1.5 km. Below this threshold the resolution limit of our simulations is reached. The 'bump' at ∼3 km marks the point where the second SFD becomes more dominant; this difference could be minimized by fine-tuning the second impact's energy.

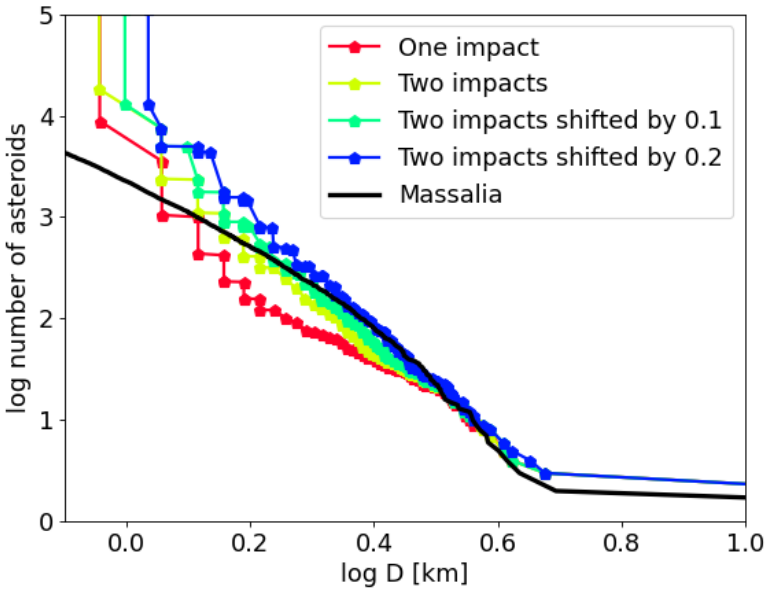

Figure 5.7 Comparison of synthetic SFDs from Fig. 5.6 to distributions from the first and second impacts, where the 2nd impact was shifted by a small amount.

slope change (2000 m, 1500 m, 1000 m, 500 m). The resulting ejected volumes and pre-impact sizes are listed in Tabs. 5.1 and 5.2.

We compared these extrapolated populations to the observed populations of 1-m L-chondrites and dust, as mentioned above. If we begin the extrapolation at 500 m, only the -2.8 slope matched the 1-m population and only slightly overshot the dust population. (Fig. 5.8 The 1000-m extrapolation needed the slope to be under -3.1, with -2.8 just reaching the dust population. The 1500-m needed slope at most -3.2, but -2.8 did not even reach the dust. As for the 2000-m shift, it needed a slope of at least -3.0 to reach the populations. Fig. 5.9 shows one of the extrapolations (1500 m, -3.1), that has both large enough 1-m population and reasonably overshoots the dust.

When comparing the matching populations and ejected volumes from Tabs. 5.1 and 5.2, we can safely eliminate the extreme cases with too low ($<$50 000 km^3) and too high ($>1 \cdot 10^6$ km^3 volumes). This makes the extrapolated original size of the target between 134 and 155 km in diameter.

Re-doing Simulations for Larger Diameters At first glance, our extrapolated results appear to contradict our previous findings, as they require significantly more ejected material (35% of the original body volume compared to only 10%), and consequently, a larger projectile.

However, this discrepancy is not surprising, as the collision is expected to produce dust and small fragments that are simply far beyond the resolution limit of our simulations. In fact, we can see a similar effect taking place in our simulations; when comparing just the low- and high-resolution simulations, we see an increase in the ejected volume by several percent of the original body volume.

One way this could be solved is by adding the missing volume in the form of additional particles, with properties of dust or metre-sized fragments, effectively adding dust clouds and groups of fragments. These would then be handled separately from the standard particles. At the same time, we expect the necessary size of projectile should be larger, up to approximately 32 km (cf. Appendix A).

Overshooting the Main Belt at 1-m Size In our extrapolations, we have encountered cases where we overshot the 1-m meteoroid and dust populations; hence, we excluded them for the second impact scenario. However, the first impact would have been more energetic and significantly overshot the current 1-m population, in order to account for the mid-Ordovician infall (Schmitz et al., 2019). Consequently, the scenarios, which were extrapolated from 500 m, could be considered as describing the first impact, 470 My ago.

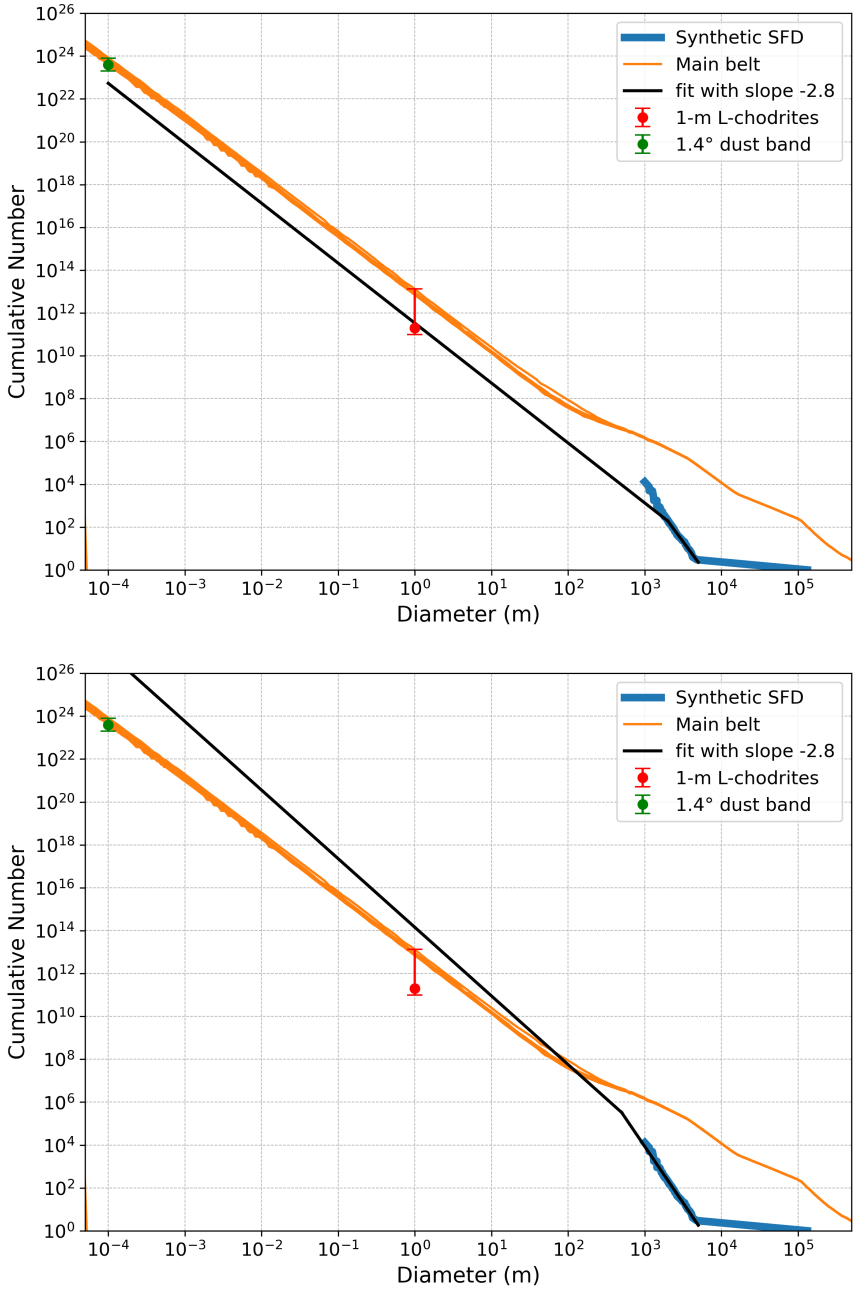

Figure 5.8 Synthetic SFDs extrapolated down to 100 μm dust particles. The population of 1.4° dust band is $4 \cdot 10^{23}$ and the expected number of 1-m L-chondrites is $10 - 30 \cdot 10^{10}$, the upper error bar is the expected population right after impact ($\sim 1.3 \cdot 10^{13}$). Examples of extrapolations of combined two-impact SFDs that undershoot (top) and overshoot (bottom) our anchor populations. For comparison, synthetic Main Belt populations from Marsset et al. (2024) are plotted in orange.

Slope	Size limit for extrapolation			
	2000 m	1500 m	1000 m	500 m
−2.8	13	24	71	**340**
−2.9	20	40	**115**	**540**
−3.0	42	**80**	**229**	1 050
−3.1	**112**	**206**	**570**	2 500
−3.2	**363**	**650**	1 750	7 200
−3.3	1 380	2 400	6 200	24 000

Table 5.1 The extrapolated ejected volume (in 10^3 km³) for various slopes and sizes, where the extrapolation begins. Extrapolations were done for the combined synthetic SFD from Section 5.2. The bold numbers correspond to extrapolations matching the dust and 1-m anchors.

Slope	Size limit for extrapolation			
	2000 m	1500 m	1000 m	500 m
−2.8	131.5	132	133.5	**142.5**
−2.9	131.8	132.5	**135**	**149**
−3.0	132.5	**134**	**139**	162
−3.1	**135**	**138**	**150**	192
−3.2	**143**	**152**	177	250
−3.3	170	190	240	364

Table 5.2 Same as Tab. 5.1, but showing extrapolated pre-impact sizes of the target (in km).

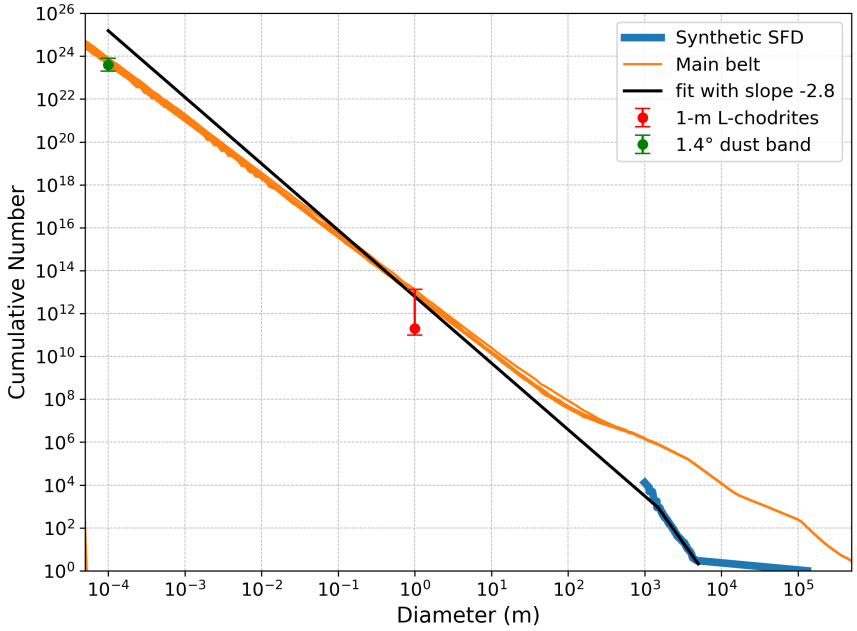

Figure 5.9 Same as Fig. 5.8, the combined two-impact SFD (bottom) is extrapolated from 1500 m sizes at slope of −3.1. It has a significant population of 1-meter bodies (close to the estimates after impact) and overshoots the dust population, leaving some space for possible dynamical evolution.

6 Impacts into Layered Body

So far, we explored two idealized scenarios, one with the target body being fully monolithic and the other with the body completely pre-damaged. In this chapter, we explore a scenario where the target body is layered; it has a monolithic core overlaid by a damaged layer of regolith (rubble-pile). Such a layout was originally motivated by the AO imaging (Fig. 3.2. We hoped to induce higher rates of ejection with a less cohesive surface layer. Hence, we performed additional simulations set up identically as in Sec. 4.1, this time with a 134-km body having 10- and 20-km layers of rubble around a monolithic core. We hit the target body with a 20-km projectile at a 45° angle; this projectile again was the one best matching the observed SFD of the Massalia family. In this case, we used the resolution of 800,000 particles.

SFD We compared the resulting SFDs from layered body impacts to the previously discussed impacts (Fig. 6.1). The 10-km layer impact shows very little difference from the fully monolithic. The only notable difference is the size of the largest fragment, which is in this case 4.2 km, compared to 5.2 km. However, we cannot exclude the possibility that this is just stochastic variability. The 10-km layer impacts did not produce significantly more or less ejected volume compared to the previous ones. (V ∼100,000 km^3 or 7.5% of the original body).

On the other hand, the SFD of the 20-km layer impact resembles the rubble-pile impact, having a very steep slope (-8.2 ± 0.2). The ejected volume from the 20-km layer impact is higher than the previous one, at ∼140,000 km or 10%.

The Largest Remnant The most significant difference in the layered impacts occurs minutes after the impact and is closely tied to the final shape of the largest remnant (Fig. 6.2). Right after the projectile hits the target, it easily ejects the material from the impact point to the sides, just like in the rubble-pile impact. However, as the monolithic core compresses and decompresses with the passing shock wave, there is a major rebound, ejecting material in the direction opposite the original projectile velocity. This rebound flow eventually forms a high central peak just in the middle of the impact crater. The original rubble pile transported material via ejection and reaccretion away from the impact point to the sides and to the antipode, revealing the original monolithic cavity at the impact point. However, the high central peak is in contradiction with the AO observations (Fig. 3.2).

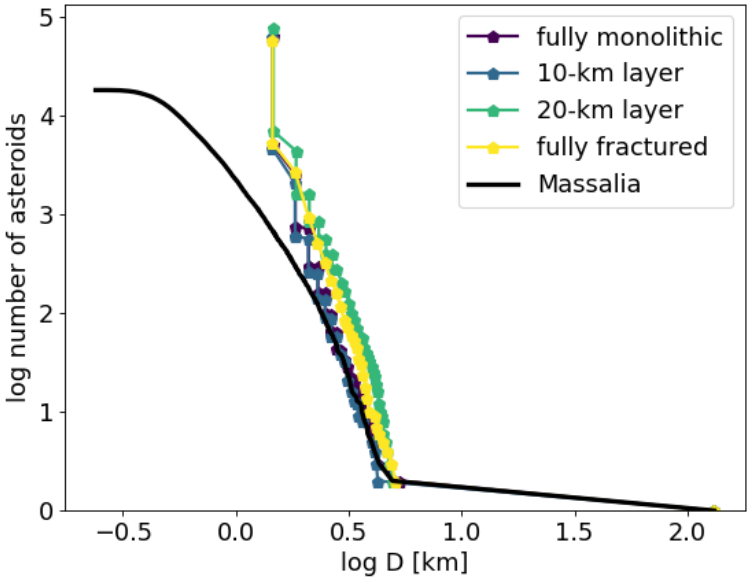

Figure 6.1 Same as Fig. 4.4, this time with a 10- and 20-km-thick layer of rubble around a monolithic core. We see that the 10-km layer has little to no effect on the SFD compared to fully monolithic body. On the other hand, the 20-km layer is much steeper, similar to the fully rubble-pile body.

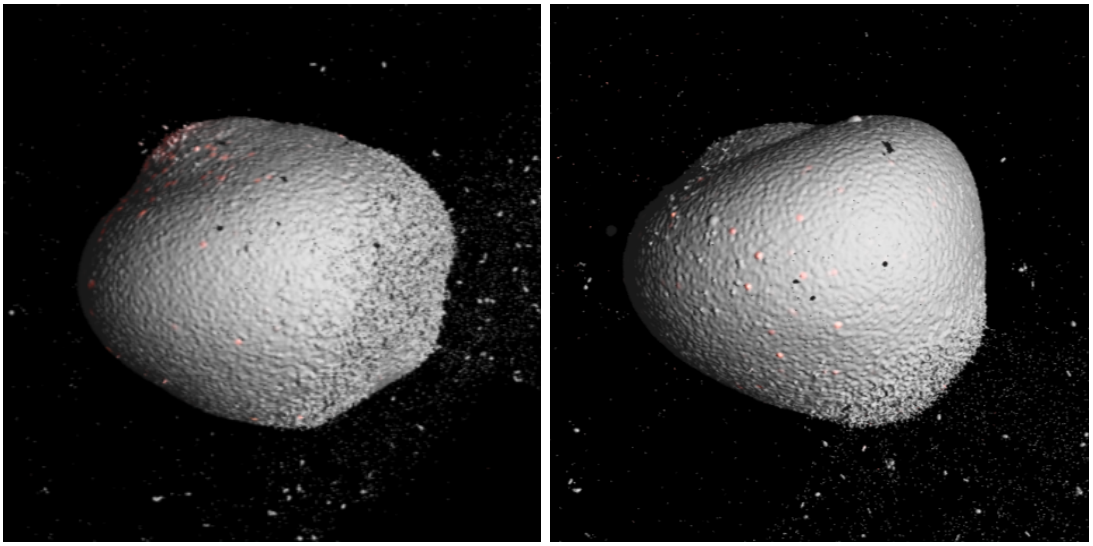

Figure 6.2 Shape of the largest remnants for impacts into the 10-km (left) and 20-km rubble-pile layer of a differentiated body (right). In both cases, there is a high central peak formed by the rebound flow.

7 Conclusions

In this work, we have theoretically explored the collisions that may have formed the Massalia family and are the origin of L-chondrite meteorites.

At first, we simulated impacts into a monolithic body, assuming it to be the first, major impact after the formation of asteroid (20) Massalia. We selected impacts with 16- and 20-km projectiles as the best candidates, using low-resolution simulations, and subsequently performed high-resolution simulations (up to 3.2 million particles, 0.9 km particle diameter). The high resolution allowed us to model the ejection of a thin surface layer, which could not be modeled at lower resolutions. The synthetic size frequency distribution (N(>D); SFD) of the 16-km impact matches the observed SFD from the largest fragment (4.8 km) to 3-km sizes; however, it was lacking for < 3 km sizes. On the other hand, the more energetic 20-km impact matched the observations well on the 1.5 to 4 km sizes but created a largest fragment significantly larger ($D = 6.5$ km) than the observed (D = 4.9 km). The ejected volumes were ∼50,000 km^3 and 110,000 km^3, respectively. The final shape of the largest remnants was flattened on one side and bulged on the other (Fig. 4.6, 4.10), differing from the AO observations by Marsset (pers. comms.), which exhibit a large, crater-like structure and an antipodal peak.

In the second part, we focused on impacts into a rubble pile, assuming that the previous impact shattered the asteroid. We again selected on 16- and 20-km impacts. The resulting SFDs were very steep, with slopes $N(> D) \approx CD^{\gamma}$ over -8. (Slope of the observed family is 5.3 ± 0.1.) The SFDs were systematically shifting towards smaller sizes; we did not achieve convergence for even our highest resolution. However, when we combined the monolithic and rubble-pile impact SFDs, as if they were subsequent impacts, we achieved a great match with the observed SFD. The second impact helped to compensate for the underpopulated (Fig. 5.7. Such impacts would in total eject from 90,000 to 125,000 km of material.

The largest remnants from the rubble-pile impacts closely resembled the AO observations. They have a wide, flattened side, with a crater-like structure and a significant antipodal peak (Fig. 5.5). This means, (20) Massalia was likely pre-damaged before its second impact, supporting the need for two subsequent impacts.

In order to account for meteoroids and dust ejected during impacts, we extrapolated the synthetic SFD down to 100 μm, with varying slopes. We compared the extrapolated populations to populations of dust and 1-m L-chondrites. The original size of the target needed to account for dust and meteoroids is from 134 to 155 km.

Future Work In order to account for the dust and meteoroids in the SPH simulations, we would have to add many more particles; however, that is not realistic. Therefore, we suggest using tracer particles, which would have special material parameters and would represent dust clouds. Then the same would go

for other fragment sizes, e.g. groups of meter-sized meteoroids. Such models could be a next step in modeling impacts.

Other than simulations accounting for dust, a possible discussion of rotational states of the fragments would be very useful, including comparison to distributions of rotational states inferred from Gaia observations (Ďurech & Hanuš, 2023). The effects of target body rotation and non-spherical shapes before impacts are closely related to this.

References

Barnes, J. E. 1986, in The Use of Supercomputers in Stellar Dynamics, ed. P. Hut & S. L. W. McMillan, Vol. 267, 175

Benavidez, P. G., Durda, D. D., Enke, B., Campo Bagatin, A., Richardson, D. C., Asphaug, E., & Bottke, W. F. 2018, Impact simulation in the gravity regime: Exploring the effects of parent body size and internal structure, Icarus, 304, 143

Benz, W. & Asphaug, E. 1993, *Explicit 3D Continuum Fracture Modeling with Smooth Particle Hydrodynamics*, in Lunar and Planetary Science Conference, Lunar and Planetary Science Conference, 99

Benz, W. & Asphaug, E. 1995, Simulations of brittle solids using smooth particle hydrodynamics, Computer Physics Communications, 87, 253

Benz, W. & Asphaug, E. 1999, Catastrophic Disruptions Revisited, Icarus, 142, 5

Berthier, J., Carry, B., Mahlke, M., & Normand, J. 2023, SsODNet: Solar system Open Database Network, Astron. Astrophys., 671, A151

Bottke, W., Meyer, A., Vokrouhlicky, D., Nesvorny, D., Bierhaus, E., Hoover, R., DellaGiustina, D., Connolly, H., & Lauretta, D. 2024, *Surface Ages for the Sample Return Asteroids Bennu, Ryugu and Itokawa*, in AAS/Division for Planetary Sciences Meeting Abstracts, Vol. 56, 56th Annual Meeting of the Division for Planetary Sciences, 105.03

Bottke, W. F., Brož, M., O'Brien, D. P., Campo Bagatin, A., Morbidelli, A., & Marchi, S. 2015, in Asteroids IV, ed. P. Michel, F. E. DeMeo, & W. F. Bottke, 701–724

Bottke, W. F., Durda, D. D., Nesvorný, D., Jedicke, R., Morbidelli, A., Vokrouhlický, D., & Levison, H. F. 2005, Linking the collisional history of the main asteroid belt to its dynamical excitation and depletion, Icarus, 179, 63

Brož, M., Chrenko, O., Nesvorný, D., & Dauphas, N. 2021, Early terrestrial planet formation by torque-driven convergent migration of planetary embryos, Nature Astronomy, 5, 898

Brož, M., Vernazza, P., Marsset, M., DeMeo, F. E., Binzel, R. P., Vokrouhlický, D., & Nesvorný, D. 2024, Young asteroid families as the primary source of meteorites, Nature, 634, 566

Brož, M. & Šolc, M. 2013, Fyzika sluneční soustavy, 1st edn. (Prague: MatfyzPress)

Cellino, A., Hestroffer, D., Lu, X. P., Muinonen, K., & Tanga, P. 2019, Inversion of HIPPARCOS and Gaia photometric data for asteroids. Asteroid rotational properties from sparse photometric data, Astron. Astrophys., 631, A67

Collins, G. S., Melosh, H. J., & Ivanov, B. A. 2004, Modeling damage and deformation in impact simulations, , 39, 217

Dahlgren, M. 1998, A study of Hilda asteroids. III. Collision velocities and collision frequencies of Hilda asteroids, Astron. Astrophys., 336, 1056

DeMeo, F. E., Binzel, R. P., Slivan, S. M., & Bus, S. J. 2009, An extension of the Bus asteroid taxonomy into the near-infrared, Icarus, 202, 160

Dohnanyi, J. S. 1969, Collisional Model of Asteroids and Their Debris, , 74, 2531

Durda, D. D., Bottke, W. F., Nesvorný, D., Enke, B. L., Merline, W. J., Asphaug, E., & Richardson, D. C. 2007, Size-frequency distributions of fragments from SPH/ N-body simulations of asteroid impacts: Comparison with observed asteroid families, Icarus, 186, 498

Ďurech, J., Hanuš, J., & Alí-Lagoa, V. 2018, Asteroid models reconstructed from the Lowell Photometric Database and WISE data, Astron. Astrophys., 617, A57

Gingold, R. A. & Monaghan, J. J. 1977, Smoothed particle hydrodynamics: theory and application to non-spherical stars., Mon. Not. R. Astron. Soc., 181, 375

Grady, D. E. & Kipp, M. E. 1980, Continuum modelling of explosive fracture in oil shale, International Journal of Rock Mechanics and Mining Sciences and Geomechanics Abstracts, 17, 147

Graf, T. & Marti, K. 1995, Collisional history of H chondrites, , 100, 21247

Heck, P., Schmitz, B., Bottke, W., Rout, S., Kita, N., Cronholm, A., Defouilloy, C., Dronov, A., & Terfelt, F. 2017, Rare meteorites common in the Ordovician period, nature astronomy, 1, 0035

Hirayama, K. 1918, Groups of asteroids probably of common origin, Astrophys. J., 31, 185

Holsapple, K. A. & Michel, P. 2008, Tidal disruptions. II. A continuum theory for solid bodies with strength, with applications to the Solar System, Icarus, 193, 283

Jedicke, R., Granvik, M., Micheli, M., Ryan, E., Spahr, T., & Yeomans, D. K. 2015, in Asteroids IV, ed. P. Michel, F. E. DeMeo, & W. F. Bottke, 795–813

Jones, R. L., Bannister, M. T., Bolin, B. T., Chandler, C. O., Chesley, S. R., Eggl, S., Greenstreet, S., Holt, T. R., Hsieh, H. H., Ivezic, Z., Juric, M., Kelley, M. S. P., Knight, M. M., Malhotra, R., Oldroyd, W. J., Sarid, G., Schwamb, M. E., Snodgrass, C., Solontoi, M., & Trilling, D. E. 2021, *The Scientific Impact of the Vera C. Rubin Observatory's Legacy Survey of Space and Time (LSST) for Solar System Science*, in Bulletin of the American Astronomical Society, Vol. 53, 236

Jutzi, M., Holsapple, K. A., Wünneman, K., & Michel, P. 2015, in Asteroids IV, ed. P. Michel, F. E. DeMeo, & W. F. Bottke, 679–699

Kaasalainen, M. & Torppa, J. 2001, Optimization Methods for Asteroid Lightcurve Inversion. I. Shape Determination, Icarus, 153, 24

Kruzins, E., Benner, L., Brown, M., Coward, D., Molera Calves, G., Edwards, P., Giorgini, J., Guedon, S., Horiuchi, S., Gendre, B., Kennewell, J., Lambert, A., Lazio, J., Linsten, B., Moore, J., Mieczkowska, D., Peters, E., Phillips, C., & Riddell, T. 2024, *Detection in Deep Space from the Southern Hemisphere of Near Earth Objects Using a Combined Radar/Optical System*, in Advanced Maui Optical and Space Surveillance (AMOS) Technologies Conference, ed. S. Ryan, 104

Libersky, L. D. & Petschek, A. G. 1991, in Advances in the Free-Lagrange Method Including Contributions on Adaptive Gridding and the Smooth Particle Hydrodynamics Method, ed. H. E. Trease, M. F. Fritts, & W. P. Crowley, Vol. 395, 248–257

Lucy, L. B. 1977, A numerical approach to the testing of the fission hypothesis., Astrophys. J., 82, 1013

Mahlke, M., Carry, B., & Mattei, P. A. 2022, Asteroid taxonomy from cluster analysis of spectrometry and albedo, Astron. Astrophys., 665, A26

Marsset, M., Vernazza, P., Brož, M., Thomas, C. A., DeMeo, F. E., Burt, B., Binzel, R. P., Reddy, V., McGraw, A., Avdellidou, C., Carry, B., Slivan, S., & Polishook, D. 2024, The Massalia asteroid family as the origin of ordinary L chondrites, Nature, 634, 561

Masiero, J. R., DeMeo, F. E., Kasuga, T., & Parker, A. H. 2015, in Asteroids IV, ed. P. Michel, F. E. DeMeo, & W. F. Bottke, 323–340

Mises, R. v. 1913, Mechanik der festen Körper im plastisch- deformablen Zustand, Nachrichten von der Gesellschaft der Wissenschaften zu Göttingen, Mathematisch-Physikalische Klasse, 1913, 582

Monaghan, J. J. 1989, On the Problem of Penetration in Particle Methods, Journal of Computational Physics, 82, 1

Nesvorný, D. & Bottke, W. F. 2004, Detection of the Yarkovsky effect for main-belt asteroids, Icarus, 170, 324

Nesvorný, D., Brož, M., & Carruba, V. 2015, in Asteroids IV, ed. P. Michel, F. E. DeMeo, & W. F. Bottke, 297–321

Nesvorný, D., Roig, F., Vokrouhlický, D., & Brož, M. 2024, Catalog of Proper Orbits for 1.25 Million Main-belt Asteroids and Discovery of 136 New Collisional Families, , 274, 25

Nesvorný, D., Vokrouhlický, D., Bottke, W. F., & Sykes, M. 2006, Physical properties of asteroid dust bands and their sources, Icarus, 181, 107

Piazzi, G. 1802, Della scoperta del nuovo pianeta Cerere Ferdinandea, ottavo tra i primari del nostro sistema solare

Pravec, P., Harris, A. W., & Michalowski, T. 2002, in Asteroids III, ed. W. F. Bottke, Jr., A. Cellino, P. Paolicchi, & R. P. Binzel, 113–122

Rubin, A. E. & Ma, C. 2017, Meteoritic minerals and their origins, Chemie der Erde / Geochemistry, 77, 325

Schmitz, B., Farley, K. A., Goderis, S., Heck, P. R., Bergström, S. M., Boschi, S., Claeys, P., Debaille, V., Dronov, A., van Ginneken, M., Harper, D. A., Iqbal, F., Friberg, J., Liao, S., Martin, E., Meier, M. M. M., Peucker-Ehrenbrink, B., Soens, B., Wieler, R., & Terfelt, F. 2019, An extraterrestrial trigger for the mid-Ordovician ice age: Dust from the breakup of the L-chondrite parent body, Science Advances, 5, eaax4184

Ševeček, P. 2021, Simulations of asteroid collisions using a hybrid SPH/N-body approach, PhD thesis, Charles University, Astronomical Institute

Ševeček, P., Brož, M., & Jutzi, M. 2019, Impacts into rotating targets: angular momentum draining and efficient formation of synthetic families, Astron. Astrophys., 629, A122

Ševeček, P., Brož, M., Nesvorný, D., Enke, B., Durda, D., Walsh, K., & Richardson, D. C. 2017, SPH/N-Body simulations of small ($D = 10\,\mathrm{km}$) asteroidal breakups and improved parametric relations for Monte-Carlo collisional models, Icarus, 296, 239

Šidlichovský, M. & Nesvorný, D. 1994, Temporary capture of grains in exterior resonances with the Earth: planar circular restricted three-body problem with Poynting-Robertson drag., Astron. Astrophys., 289, 972

Springel, V. 2010, Smoothed Particle Hydrodynamics in Astrophysics, Annu. Rev. Astron. Astrophys., 48, 391

Swindle, T. D., Kring, D. A., & Weirich, J. R. 2014, $^{40}\mathrm{Ar}/^{39}\mathrm{Ar}$ ages of impacts involving ordinary chondrite meteorites, Geological Society of London Special Publications, 378, 333

Tillotson, J. H. 1962, Metallic Equations of State For Hypervelocity Impact, General Atomic Report GA-3216. 1962. Technical Report

Ďurech, J. & Hanuš, J. 2023, Reconstruction of asteroid spin states from Gaia DR3 photometry, Astron. Astrophys., 675, A24

Vernazza, P., Ferrais, M., Jorda, L., et al. 2021, VLT/SPHERE imaging survey of the largest main-belt asteroids: Final results and synthesis, Astron. Astrophys., 654, A56

Vokrouhlický, D., Bottke, W. F., Chesley, S. R., Scheeres, D. J., & Statler, T. S. 2015, in Asteroids IV, ed. P. Michel, F. E. DeMeo, & W. F. Bottke, 509–531

Vokrouhlický, D., Čapek, D., Kaasalainen, M., & Ostro, S. J. 2004, Detectability of YORP rotational slowing of asteroid 25143 Itokawa, Astron. Astrophys., 414, L21

Walsh, K. J. 2018, Rubble Pile Asteroids, Annu. Rev. Astron. Astrophys., 56, 593

Weibull, W. 1939, A Statistical Theory of the Strength of Materials, Ingeniörsvetenskapsakademiens handlingar, 151, generalstabens Litografiska Anstalts förlag

Zhang, T. A., Liao, S., Wu, R., & Schmitz, B. 2024, L-chondrite body breakup in Ordovician strata in China - A time tie point globally and across the inner solar system, Earth and Planetary Science Letters, 643, 118891

A List of Low-resolution Simulations Parameters

Monolithic			
R_{target} [km]	$R_{\text{projectile}}$ [km]	v_{impact} [km/s]	Impact angle [°]
67	6	5	15
67	6	5	30
67	6	5	45
67	7	5	45
67	8	5	0
67	8	5	15
67	8	5	30
67	8	5	45
67	8	5	60
67	9	5	45
67	10	5	45
67	10	5	60
67	11	5	45
67	12	5	45
67	12	5	60
67	14	5	45
67	8	3	45
67	10	3	45
67	12	3	45
67	14	3	45
67	5	7	45
67	6	7	45
67	7	7	45
67	8	7	45
67	6	10	45

Table A.1 List of simulation parameters for low-resolution simulation used for impacts into a monolith.

Rubble-pile			
R_{target} [km]	$R_{\text{projectile}}$ [km]	v_{impact} [km/s]	Impact angle [°]
67	6	5	45
67	7	5	45
67	8	5	45
67	8	5	0
67	8	5	15
67	8	5	30
67	8	5	60
67	9	5	45
67	10	5	45
67	12	5	45
67	14	5	45
67	16	5	45
67	18	5	45
67	20	5	45
67	22	5	45

Table A.2 Same as Tab. A.1, but for rubble-piles.